Chapter 2

Overview of the characterisation techniques

An exact control of the structure and composition of the active films is a prerequisite for the preparation of high-quality materials for photovoltaic applications. In addition, any further improvement on the state-of-the-art device performance requires a profound knowledge of the mechanisms governing the electronic transport and the identification of those factors limiting its operation. With this aim, different complementary techniques have been employed in the frame of this work for the structural and electronic characterisation of thin-films and solar cells based on CVD-grown $CuGaSe_2$ (CGSe). In this chapter the basics of these techniques will be reviewed, whose actual application to the case of study will be discussed in the following chapters.

For the sake of clarity, the characterisation techniques have been divided into three categories. In Section 2.1, those techniques used for the structural and/or compositional characterisation of CGSe-films and related devices will be reviewed, although in some cases (e.g. in photoemission studies) the electronics of films and devices are also surveyed. They include the electron microscopy in various modalities, namely Scanning Electron Microscopy (SEM), Electron Microprobe for Energy Dispersive X-ray analysis (EDX), and Transmission Electron Microscopy (TEM), which constitute the set of structural characterisation techniques used in this work based on electron irradiation of the samples under study. Section 2.1 is completed with three techniques based on the use of photons as probe beam, X-Ray Diffraction (XRD), X-Ray Fluorescence spectrometry (XRF) and photoelectron spectroscopy (XPS and UPS).

In Section 2.2 the basics of those techniques used for the electronic characterisation of devices will be summarised. The exposition will be more detailed than in the preceding section, as analytical models of the electronic transport associated to these techniques will also be reviewed for their subsequent application in Chapters 3 and 4. These techniques include the analysis of the Electron-Beam-Induced Current (EBIC), current-voltage characteristics as a function of illumination and temperature I(V,T) and the Quantum Efficiency (QE) of complete devices, from which valuable information can be gained on the electronic transport mechanisms governing the performance of the solar cells. Contrarily to the structural characterisation methods mentioned above, which are carried out on the basis of commercial equipments, the methods used in this work for the electronic characterisation make use of home-made set-ups (except the EBIC method, based on a commercial SEM), whose main features will be highlighted in Sections 2.2.2 and 2.2.3.

The Chapter is completed with a brief introduction to the Kelvin Probe Force Microscope (KPFM) in Section 2.3, which provides a bridge between the electronic and structural characterisation in the nanometre scale.

2.1 Tools for the structural characterisation

The characterisation techniques employed for the structural and compositional analysis of the different layers forming the devices under study share some common basic features, despite of the fact of requiring different set-ups (including different sample preparations) and making use of different physical processes. All of them consist in the excitation of the sample by irradiating it with a probe beam, consisting either of electrons or photons, which induces a number of electronic transitions and related relaxation processes within a certain generation volume in the sample, whose shape and size depends in turn on the energy of the incident beam and on material properties, like its density or ionisation cross-section. These processes typically result in the scattering of the primary beam and/or the re-emission of either electrons or photons from the sample, the detection of which constitute what is referred to as the actual measurement. Figure 6 and 7 show schematically the typical processes induced on the sample by an incident electron beam. Similar processes are induced by X-rays acting as primary beam, except the scattering and transmission of electrons and the Bremsstrahlung. In the following sections the basics of those structural characterisation techniques based on electron and photon beams used in this work will be reviewed.

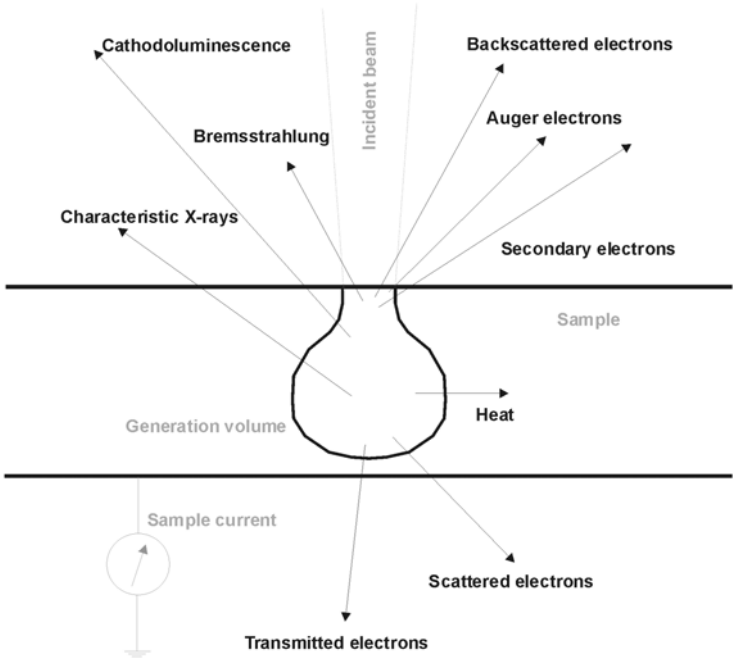

Figure 6. Schematic illustration of the main processes resulting from the interaction of an electron beam with a sample. Similar processes result from the interaction of X-rays as incident beam, excluding those of Bremsstrahlung and scattered, backscattered and transmitted electrons. The generation volume is a function of the incident beam energy and of the material properties. Samples are normally grounded to avoid charging effects due to electron release. The resulting net current can be measured, as shown in the diagram.

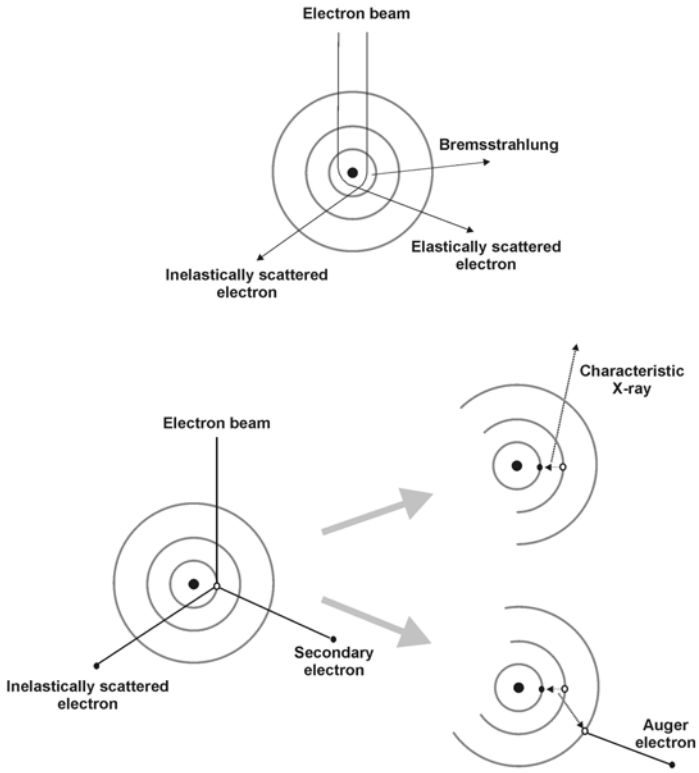

Figure 7. Schematic model of different processes included in Figure 6. **(Top)** Elastic and inelastic electron scattering by the positively charged atomic nucleus. The electron energy loss related to inelastic processes is emitted as Bremstrahlung. **(Bottom)** The impinging electron ionises the sample atom, ejecting an inner-shell electron (secondary electron). Subsequently, two possible relaxation processes can occur, involving either the emission of characteristic X-rays, or the emission of an Auger electron. Secondary electrons are used in SEM and XPS (in the later case using photons as primary beam), whereas characteristic X-rays are detected in EDX and XRF analysis (the latter by means of photons as primary beam); Auger electrons form the basis of Auger spectroscopy; and inelastically scattered electrons appear as background in SEM and XPS measurements (see text).

2.1.1 The electron microscope (SEM)

Following de Broglie's statement on the wave-particle duality, the principles of optical microscopy can be applied to entities traditionally conceived as particles, like electrons. For the use of electrons as probes, optical lenses in conventional optical microscopes must be replaced by their electromagnetic equivalents, whose function is to focus the electron beam on the sample by means of electromagnetic interactions, derived from Lorentz's force. The pioneering work of Ruska[71] on electromagnetic lenses led to the construction of the first electron microscope. The main goal of that work was to overcome the limitations imposed to the image magnification in optical microscopy by the use of visible light as probe. As the associated wavelength of a particle is inversely proportional to its velocity, it became clear that highly accelerated electrons were a convenient probe for replacing visible light in high-resolution microscopy. From the expression of the kinetic energy E_{kin} of a particle with momentum **p** as a function of the associated wavelength, including relativistic corrections:

$$E_{kin} = \frac{p^2}{2m_e} = \frac{4\pi^2\hbar^2c^2}{2m_ec^2}\frac{1}{\lambda^2} \qquad \text{Eq. 33}$$

it follows that wavelengths below 0.005 nm can be obtained with electrons accelerated by 60 kV. In practice, the resolution of an electron microscope is limited by the aberration of the electromagnetic lenses, rather than by the wavelength of the accelerated electrons.

Generally speaking, electron microscopes can be roughly classified in three categories, depending on the specific product of the electron-beam/sample interaction analysed. These are:

- Scanning electron microscopes (SEM), which are based on the detection of secondary electrons.
- Electron microprobes, based on the analysis of characteristic X-rays emitted from the sample
- Transmission electron microscopes (TEM), which detect electrons transmitted through thin samples.

All three types of techniques share some common features. They consist of an electron column operated under high vacuum, where electrons generated from a source (typically a tungsten filament, a lanthanum hexaboride LaB_6 emitter or a field-emission gun) are accelerated by means of an applied voltage (normally in the range of 5-40 kV in SEM and microprobes, between 100-300 kV in TEM). A set of electromagnetic lenses focuses the beam on the sample, which is mounted on a metallic sample holder and grounded in order to avoid sample charging.

Nowadays commercial equipments include SEM and electron microprobe facilities in a single set-up, blurring the distinction between both categories. SEMs are designed to provide images of high spatial resolution. The image is created by scanning the focused electron beam in a raster pattern across the area of the sample. Secondary electrons are collected by a detector, generating a signal which is displayed in a monitor (essentially a second electron column). A general introduction to SEM and EDX principles can be found in Ref. [72]

SEM measurements were performed in this work with a LEO440 microprocessor-controlled scanning electron microscope, of the conventional three-lenses type with acceleration voltages up to 40 kV and a hairpin or LaB_6 cathode. It has a resolution of 4nm at 25 kV and is equipped with a standard SE detector, a four quadrant semiconductor detector for back-scattered electrons and a X-ray spectrometer for EDX analysis.

2.1.2 Energy Dispersive X-ray analysis (EDX)

Electron microprobes are designed to deliver stable beam currents with high intensities, in order to generate sufficient characteristic X-ray signals for practical analysis. They can include scanning capabilities, providing compositional mappings on particular

regions of the sample under study, which can be combined with SEM images, as will be shown in Chapter 3.

When electrons of appropriate energy impinge on a sample, they induce emission of characteristic X-rays, in what is essentially the inverse process of the photoelectric effect. The incoming electron ejects a secondary electron from an inner shell of a sample atom, an event which is followed by the relaxation of the excited atom by filling the core hole with a third electron from a higher electronic level, as shown in Figure 7. The electronic transition from a high- to a low-energy level is accomplished by the emission of a photon hν with the corresponding energy difference, following:

$$E_i - E_f = h\nu \qquad \text{Eq. 34}$$

where E_i and E_f denote the energy of the initial and final electronic states, respectively. The corresponding energy range of transitions involving core levels lies typically in the range of X-rays. This radiation is analysed energy-dispersively (i.e. sorted electronically and not by means of a diffraction crystal, or wavelength-dispersively) in the EDX detector. This is normally a semiconductor detector, in which a charge pulse is created by the incoming X-ray, converted into a voltage pulse afterwards and in turn into a digital signal or count to be added to the corresponding channel of a multichannel analyser. As there are different potential vacancy-filling mechanisms (as many as the different combinations of electronic transitions in the characteristic spectrum of the sample, schematically shown in Figure 8), a pattern of characteristic X-ray peaks with various energies will be recorded in a standard EDX measurement. The mean goals of EDX analyses are therefore, the identification, on the one hand, of the elements present in the sample by their characteristic X-ray pattern; and on the other hand the quantitative analysis of the sample composition, as the X-ray emission intensity will be directly related to the number of characteristic transitions taking place at each particular energy.

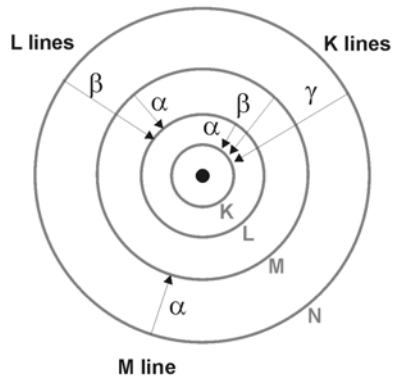

Figure 8. Line types typically observed in X-ray spectra, omitting the level multiplicity of inner shells for the sake of clarity.

2.1.3 Transmission electron microscopy (TEM)

Transmitted electrons can be analysed, as sketched in Figure 6, if the sample thickness lies below the mean free path of the electron travelling in the sample. This normally requires a laborious sample preparation, in order to provide specimens with a thickness not larger than a few tens of nanometers. Even the term thin film, used in this work to denote a semiconductor film thickness well below the typical width of a Si wafer, turns out to be inappropriate in this case, as dimensions of the order of a micron (the typical thickness of a CGSe absorber film) greatly exceed the required sample thickness for practical TEM studies. A detailed introduction to the technique can be found in Ref. [73].

For this purpose, pieces of the samples to be studied were cut and glued face-to-face in pairs with conductive epoxy, in order to avoid sample charging during the measurement. This method provides an even sample hardness distribution for the subsequent thinning, as otherwise those softer compounds in the multilayer structure making up the solar cell can be preferentially removed during processing. Additionally, the total sample area to be prepared from a single preparation is doubled, thus increasing the likelihood of finding adequate areas for TEM analysis across the sample. The preparation proceeds with the thinning of the sample by polishing with a diamond abrasive wheel and alumina paste, and a final milling stage with Ar^+ ions.

Two different commercial TEM set-ups have been used in this work for the structural analysis of CGSe-based thin-film solar cells. Both TEM equipments, a Phillips CM12 and a Phillips CM200, included EDX units for the compositional analysis of samples, in point and scanning operation modes. The microscopes were operated respectively at 120 and 200 kV for high-resolution (HRTEM) imaging.

2.1.4 X-ray diffraction (XRD)

A mandatory condition of any survey technique reads that the sampling probe must count with a scale bar of the same dimensions of the sample under investigation. Photons are routinely used as probes, as they can be conveniently characterised by their wavelength, an intrinsic scale bar. Since the wavelengths of X-ray photons are of the same dimensions as the lattice parameters of crystals, X-rays constitute a powerful tool for the structural characterisation of crystal lattices, as already pointed out by von Laue in 1913[74]. The fundamental physical process involved when a plane wave of X-rays impinges on a perfect crystal lattice, where atoms are arranged in the three spatial dimensions in a periodic way, is the diffraction of the primary beam by these atoms acting as diffraction centres. Constructive and destructive interference of diffracted beams result in the outgoing X-rays being constrained along certain directions, holding certain angles with the incident beam. Two equivalent analysis of the X-ray diffraction by periodic arrays of atoms were developed by von Laue[75] and Bragg[76] (for a general review in the frame of solid-state physics, see for instance Ref. [77]) and both have been routinely used by crystallographers for the determination of crystal structures. The

basics of the X-ray diffraction method will be briefly summarised, following the analysis of Slater[78], which highlights the equivalency of Laue and Bragg approaches.

The incoming X-ray to be scattered can be described by the real part of a plane wave, $\exp[i(\omega_o t-\mathbf{k}_o\mathbf{r})]$, where ω_o is the angular frequency, $\mathbf{k}_o$ the propagation vector and $\mathbf{r}$ is the position. The scattering element can in turn be written analogously as the real part of $\exp[i(\omega_1 t-\mathbf{k}_1\mathbf{r})]$. In the case of Laue/Bragg scattering, the sinusoidal component of the scattering centre corresponds to the stationary electron density, to act as diffraction centre in the crystal lattice, with $\omega_1=0$ and $\mathbf{k}_1$ representing the particular Fourier component of the lattice vector (i.e. a vector of the reciprocal lattice, following Laue's approach). Now, the interaction between the two waves can be represented by a scattered wave given by the real part of $\exp\{i[(\omega_o\pm\omega_1)t-(\mathbf{k}_o\pm\mathbf{k}_1)\mathbf{r})]\}$, whose amplitude will be determined by the scattering properties of the specimen, including the amplitude of a structure factor accounting for the geometrical disposition of the scattering centres in the periodic array, and an atomic factor related to their electronic density[e]. As $\omega_1=0$, as stated above, the angular frequency of the scattered wave is the same as that of the incoming wave (elastic scattering). This requires that the propagation vector $\mathbf{k}_s= \mathbf{k}_o\pm\mathbf{k}_1$ of the scattered wave must have the same magnitude as the propagation vector of the incident wave $\mathbf{k}_o$, which is an equivalent statement to Bragg's formulation of diffraction. Furthermore, expressing the propagation vectors for the case $\mathbf{k}_s= \mathbf{k}_o+\mathbf{k}_1$ as:

$$k_o = \frac{2\pi}{\lambda} \qquad \text{Eq. 35}$$

$$k_1 = \frac{2\pi}{d} \qquad \text{Eq. 36}$$

where λ denotes the wavelength of the incoming wave and d the spacing between wave fronts of the stationary electron density (or equivalently, the spacing between lattice planes), simple geometrical considerations summarised in Figure 9 lead to Bragg's law of X-ray diffraction:

$$n\lambda = 2d\sin\theta \qquad \text{Eq. 37}$$

where the index n has been included to account for higher order scattering and θ is the incidence angle of the impinging X-ray with respect to the sample surface.

[e] Phases have been omitted in the discussion of the interacting waves. The fact that XRD analysis is not based on the measurement of diffracted beam amplitudes, but of their intensities (squaring the amplitude, and thus losing the information contained in the phase), prevents the acquisition of electron density maps from the samples under study, being the origin of the so-called *phase problem*.

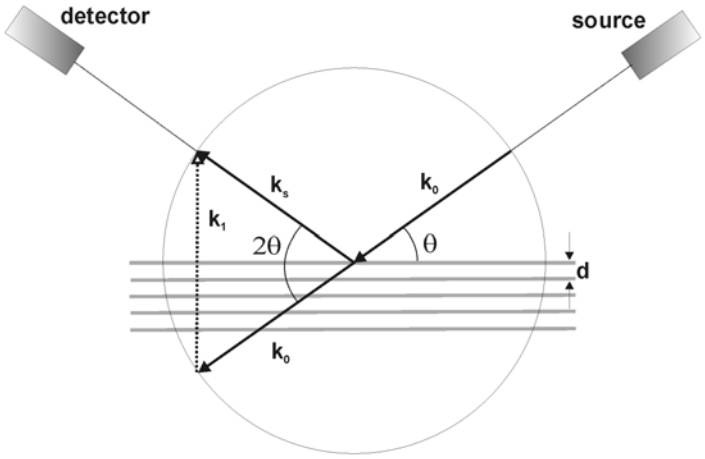

Figure 9. Schematic representation of the XRD measurement principle and the geometry involved in the derivation of Bragg's law. Crystal lattice planes with spacing distance d act as diffraction centres for the impinging X-rays emitted from a source. Bragg's law is fulfilled for scattered propagation vectors $\mathbf{k_S}$ with the same modulus as the corresponding vector of the incoming ray $\mathbf{k_0}$ (elastic scattering) and if $\mathbf{k_1} = \mathbf{k_S}-\mathbf{k_0}$, where $\mathbf{k_1}$ is a vector of the reciprocal lattice.

XRD on CVD-grown CGSe films has been applied in a previous work[79], to which the reader is referred for further details on the technique (see also Ref. [80]) and on the particular case of study. In the frame of this work, XRD has been used for the identification of secondary phases other than the expected CGSe as a function of the sample deposition conditions, and results will be presented in Chapter 3. The measurements were performed with a Bruker diffractometer, operated at 40 kV and 40 mA with CuK_α as excitation source.

2.1.5 X-Ray Fluorescence (XRF)

As alluded above, X-ray photons interact with sample atoms, as electrons do. Such interactions form the basis of the X-ray fluorescence spectrometry (XRF), by which core holes are created by the exciting radiation and relaxing processes refill the vacancies with electrons from higher shells, as in the case of EDX analysis. However, due to the large penetration depth of X-rays compared to that of electrons, this method allows to measure not only the composition of the sample, but also the total mass of each of the elements contained in the sample, being specially suitable for the analysis of multilayer structures. The electromagnetic radiation emitted by the electronic transitions (in most cases K_α- or L_α-lines –see Figure 8–, as they are the most intense lines in the spectra) is detected and used for the chemical analysis. This is based on the intensity of the recorded lines, which has the general expression for thin films[81]:

$$I = C_i K(\lambda_0)\rho d \qquad \text{Eq. 38}$$

where C is the mass fraction of the element i in the sample, ρ is the sample density, d its thickness and K is a factor which depends on the incident wavelength λ_0. Eq. 38 states that the measured intensity of the characteristic X-ray is directly proportional to the total

mass of the given element in the film. The typical sample thickness in this work, even including complete heterostructures (in the range of few microns) is small compared to the information depth of K-lines of the elements present in the sample[f], converting XRF on thin films into a bulk-sensitive characterisation tool. Furthermore, XRF provides valuable information of the thickness of layered structures, as will be shown in Chapter 3, if the corresponding material densities are known, excluding the influence of grain boundaries, surface roughness and those matrix effects associated to composition gradients. All these factors provide a higher resolution in the composition determination of samples studied by means of XRF, compared to those based on EDX analyses (in this work, typical resolutions for Cu, Ga and Se contents read ~0.3 at% for XRF and ~7 at% for EDX).

XRF measurements were performed in this work with a Phillips MagicsPRO system, implemented with a software package (FP-Multi) for the automatic analysis of the experimental data of the layered structures investigated. Information on the composition and film thickness of each component of the heterostructure could be obtained, and results will be presented in Chapter 3 in relation to the appearance and identification of interfacial phases.

2.1.6 Photoelectron spectroscopy (XPS and UPS)

Photoelectron spectroscopy is based on the photoelectric effect[82], by which a sample that is irradiated with light of sufficient energy emits electrons. According to basic quantum mechanics, and within the independent particle approximation, the absorption of a photon with energy hν by the sample induces an electronic transition according to:

$$h\nu = E_f - E_i \qquad \text{Eq. 39}$$

where E_f and E_i denote the energy of the final and initial electronic states. In a photoemission experiment, the electron originally occupies an electronic state belonging to the discrete spectrum that characterises the sample under investigation. The final state in turn belongs either to the unoccupied part of the discrete spectrum or to the continuum of electronic states above the vacuum level, the latter ones being characterised by the kinetic energy of the free electron. It is therefore possible to obtain information on the initial states of the photoemitted electrons from the analysis of their kinetic energy, when exciting the sample with photons of sufficient energy. The electron binding energy in the initial state can be determined from the energy conservation statement of the elastic process:

$$E_{kin} = h\nu - \Phi - E_B \qquad \text{Eq. 40}$$

[f] The characteristic information depths of K_α^{Cu}, K_α^{Ga}, and K_α^{Se} lines are 63 μm, 39 μm, and 38 μm, respectively, see Ref. [81].

where E_{kin} denotes the kinetic energy of the emitted electron, Φ is the work function of the electron energy analyser[g], and E_B is the binding energy of the core level.

Since its first developments in the 1950's[83], photoemission has become one of the most widely used characterisation techniques for material surfaces, in any of its versions, X-ray photoelectron- (XPS), Auger- and Ultraviolet photoelectron- (UPS) spectroscopies.

- In core-level **XPS** the intensity of those photoelectrons emitted by the sample is measured as a function of their kinetic energy, and typically plotted as a function of the electron binding energy, following Eq. 40, as will be shown in Chapters 4 and 5. Photoemission peaks are labelled according to the quantum numbers of the corresponding original level, following the standard spectroscopic notation (orbital momentum l = 0, 1, 2… denoted as *s*, *p*, *d*…). All levels with $l \geq 1$ show the corresponding spin-orbit splitting, appearing in the spectrum as a doublet with characteristic intensity ratios (determined by the multiplicity of the corresponding levels 2J+1, where J is the total angular momentum) and energy separation (characteristic of the element).
  The typical probing depth of XPS lies below 10 nm, depending on the kinetic energy of the photoelectron. This in turn means that only the first few unit cells of crystalline samples are probed in photoemission experiments, resulting in an extremely sensitive method for surface characterisation. The case in which the composition of a given sample is not homogenous is indeed frequent, with special mention to chalcopyrites, commonly showing large deviations from bulk stoichiometry values at their surfaces, as discussed in Section 1.1. This fact constitutes a critical issue for the application of these materials to photovoltaics. For this reason, and due to its high-sensitivity, photoelectron spectroscopy has been applied extensively to the study of the surface of these compounds[53].
  The chemical environment of the elements present in the sample can also be studied by XPS. The characteristic binding energies of photoelectrons are not only element specific, but also depend on the chemical state of the corresponding atom. Chemical shifts are recorded as a displacement (typically in the range of 0 to 3 eV) in binding energies of photoelectrons excited from atoms in a compound compared to the energies of the corresponding pure substance. Binding energies increase, e.g., with the oxidation state of a substance, as part of the electronic density is transferred to the oxidising species, leaving the remaining electronic density unbalanced against the positive nuclear charge.

- In addition to characteristic peaks corresponding to discrete levels at characteristic energies E_B, the XPS spectrum contains additional **Auger** peaks arising from relaxation processes of photoionised atoms by Auger transitions[84]. After emitting the photoelectron, the excited atom relaxes by filling the core hole with an electron from a higher occupied level. The energy release is accomplished either by emission of X-ray photons (X-ray fluorescence) or by the emission of a second electron, the Auger electron, as shown in Figure 7. The atomic number of the excited atom determines which of the two competing

[g] In a conventional analysis chamber, both the sample and the spectrometer are in electrical contact. This aligns their Fermi levels, providing a convenient *zero* energy reference, but their work functions differ. The emitted electron needs an amount of energy equal to the sample work function to reach the *local* vacuum level, but it will still be accelerated or decelerated by the work function difference between sample and analyser in order to reach the detector.

processes results in a higher yield. For low atomic numbers, Auger emission is favoured and the fluorescent yield is low. Conversely, higher atomic numbers favour the emission of characteristic X-rays. Auger electrons have characteristic kinetic energies corresponding to the spectrum of the specific species under study and independent of the exciting energy. The notation of Auger transitions follows the X-ray level nomenclature, as shown in Figure 8 (levels denoted as K, L, M, N…), giving, in this order, the initial core level hole, the level from which the hole is filled and the level from which the Auger electron is emitted (e.g. KL_1L_2). Valence states are denoted by V (e.g. MVV).

- **UPS** is particularly useful for the study of valence electrons, as the exciting energy is limited to some tens of eV. Typical sources of UV radiation used in UPS analysis are He I (21.2 eV) and He II (40.8 eV) lines of a discharge lamp. The method provides a practical way for the measurement of the sample work function. In a metal, the total width of the UPS spectrum U is limited by those electrons at the Fermi level (the ones having the highest kinetic energy $E_{kin} = h\nu - \Phi$) and the secondary electrons at the spectrum cut-off (the ones having the lowest energy $E_{kin} = h\nu - \Phi - U = 0$). Therefore:

$$\Phi = h\nu - U \qquad \text{Eq. 41}$$

In the case of semiconducting samples, the density of states at the Fermi level is negligible compared to that at the valence band. Thus, the UPS spectrum edge at low binding energies does not correspond now to the Fermi level, but to the uppermost valence band. The energy between the Fermi level and the uppermost valence band E_F-E_V is also a parameter of interest, as it is related to the effective doping concentration of the sample, according to Eq. 3. Examples will be shown in Sections 4.1 and 5.2.
UPS and XPS both image the density of occupied states of the sample, although not entirely in the same way. In XPS the photoemitted electrons originating from the valence band leave the sample with kinetic energies above 1 keV. In UPS the corresponding kinetic energies are typically between 5 and 40 eV and the final state may still belong to the unoccupied part of the density of states. As a result, the UPS spectrum represents a convolution of occupied and unoccupied states, and will strongly depend on the excitation energy. By increasing the photon energy, the spectrum will approach the real density of occupied states of the sample, but normally at the expense of a lower resolution, due a the broader line width of the photon source.
The unoccupied part of the density of states can be measured by Inverse Photoemission Spectroscopy (IPS)[85] in what is essentially the inverse of a photoemission process. In IPS the sample is bombarded with a beam of low energy electrons, which are incorporated into unoccupied states, from where they relax down to the Fermi level by emission of photons. The measurement of the emitted radiation as a function of the incident electron energy gives the density of unoccupied states. IPS has been applied to CVD-grown CGSe samples[50] providing complementary information to standard UPS. Of considerable interest is the possibility of estimating the energy band gap at the sample surface by combining both types of measurements, as will be discussed in Chapter 4.

2.2 Tools for the electronic characterisation

The electronic characterisation of thin-film solar cells based on CVD-grown CGSe has been carried out by means of electron-beam-induced current, current-voltage analysis under different temperatures and illumination conditions, and quantum efficiency measurements. These complementary techniques provide detailed information on the electronic transport mechanisms governing the performance of the solar cells, and their combination constitutes a powerful tool for the device diagnosis, as will be shown in the following.

2.2.1 Electron-beam induced current method (EBIC)

The incident electron beam of a SEM can generate electron-hole pairs in a piece of semiconductor, in a similar way as the sunlight does. The generation process takes place in this case by impact ionisation, creating free electrons in the conduction band and holes in the valence band of the sample under study. If the sample consists of a p-n junction, its performance can be monitored by the charge collection of the minority carriers generated by the beam. This can be done, as schematically shown in Figure 6, by measuring the current flowing through the device under short-circuit conditions (i.e. closing the loop between the front and rear contacts of the p-n junction and measuring the current). The measured current is analogous to the photocurrent, but results from electron irradiation instead of optical illumination.

The collection efficiency of generated minority carriers $\Sigma(E_b)$ is given by the general expression:

$$\Sigma(E_b) = \int_0^\infty F(x)g(E_b, x)dx \qquad \text{Eq. 42}$$

where F(x) denotes the collection probability as a function of the sample depth x where carriers are generated, and $g(E_b,x)$ is the generation function of minority carriers at a certain beam energy. The distribution of the generation volume in the semiconductor can be experimentally measured[86] or simulated[87] for a given material irradiated with a particular excitation energy, and it generally differs from the generation function that is obtained by illuminating the semiconductor with super-band gap light. An empirical expression for the radius of the generation volume R_g induced by an electron beam was first reported by Grün[88], that reads (for R_g in μm and E_b in keV):

$$R_g = \frac{4.28 \cdot 10^{-6}}{\rho} E_b^{1.75} \qquad \text{Eq. 43}$$

where ρ is the density of the material given in g/cm^3. This expression must be corrected for the case of a semiconductor heterojunction, as different materials contribute to the generation of pairs. Furthermore, the metallic rear contact is a source of backscattered primary electrons that can have a second chance to generate electron-hole pairs. A

general model for the simulation of EBIC profiles in thin-film heterojunctions was reported by Scheer[89], which is followed in this work. Experimentally, the EBIC $I_c(E_b)$ is measured under short-circuit conditions, being related to the collection efficiency according to:

$$\Sigma(E_b) = \frac{\eta\xi}{1-k}\frac{E_g I_c}{E_b I_b} \qquad \text{Eq. 44}$$

where E_g is the band gap of the absorber film and the product ξE_g denotes the energy required for the electron-hole pair generation by impact ionisation, I_b is the beam current, k is the fraction of backscattered electrons and η is a dimensionless factor that accounts for surface recombination and shunt effects, which are independent of the beam energy[90]. Due to the different impact of these parameters on the measurement of different samples, it is thus convenient to evaluate the shape of the Σ vs. E_b profile, rather than absolute values of Σ, in comparative studies. Substituting Eq. 44 in Eq. 42 and including the profile of the generation function via an expression as Eq. 43, it is possible to extract valuable information on the performance of the junction from the calculated collection probability F(x). The latter is a function exclusively of the sample under investigation, which for the case of a heterojunction will be given by:

$$F(x) = F_w + F_{SCR} + F_{abs} \qquad \text{Eq. 45}$$

where F_w denotes the local collection probability in the window layer, F_{SCR} in the space-charge region and F_{abs} in the quasi-neutral region of the absorber. While F_{SCR} is assumed to be unity (i.e. any carrier generated within the SCR is swept by the electric field without recombination), F_w is assumed to be zero due to the small minority carrier lifetime in the window layer, resulting from its high doping density. An analytical expression is required for F_{abs}, in the quasi-neutral region of the absorber, where the carrier transport is controlled by diffusion. This can be done by solving the diffusion equation in one dimension (see for instance Ref. [57]):

$$\frac{d^2F_{abs}(x)}{dx^2} - \frac{F_{abs}(x)}{L_e^*} = 0 \qquad \text{Eq. 46}$$

where L_e^* denotes the minority carrier (electron) diffusion length, including effects associated to grain boundaries. The boundary conditions of this problem read:

$$F_{abs}(w) = 1 \qquad \text{Eq. 47}$$

$$\left.\frac{dF_{abs}(x)}{dx}\right|_{x=d} = -\frac{S}{D}F_{abs}(x) \qquad \text{Eq. 48}$$

where w denotes the extension of the SCR, d is the absorber thickness, S the interface recombination velocity at the back contact and D the diffusivity of the carriers. With these boundary conditions the solution of Eq. 46 is given by:

$$F_{abs}(z) = \frac{\frac{1}{L_e^*}\cosh\left(\frac{z-d}{L_e^*}\right) - \frac{S}{D}\sinh\left(\frac{z-d}{L_e^*}\right)}{\frac{S}{D}\sinh\left(\frac{d-w}{L_e^*}\right) + \frac{1}{L_e^*}\cosh\left(\frac{d-w}{L_e^*}\right)} \qquad \text{Eq. 49}$$

The collection efficiency can thus be numerically simulated from the substitution of Eq. 49 in Eq. 42 for the right choice of parameters. A fitting procedure has been implemented[91] for this purpose, from which collection function profiles can be depicted based on fitted parameters of w and L_e^*. Experimental examples of CGSe-based solar cells will be given in Chapter 4.

EBIC experiments have been performed in this work on complete solar cells in planar configuration (i.e. with the incident beam falling on the front surface of the cells) using a scanning electron microscope (Cambridge Instruments 250 MKIII) at room temperature. The beam energy was varied between 8 and 40 keV and the beam current was correspondingly adjusted between 50 and 160 pA in order to preserve a constant electron-hole pair generation density. The measurement of the collection current was performed using a high-precision ampere-meter in short-circuit. Further experimental details can be found in Refs. [92,93].

2.2.2 Current-voltage characteristics I(V, T)

Current-voltage characteristics, referred to as I-V or J-V, depending on whether speaking of total current [A] or current density [Acm^{-2}] as a function of the applied voltage, are a standard characterisation method of the performance of electronic devices in general and solar cells in particular. Measurements performed on cells keeping the sample in darkness, hereafter referred to as *dark I-V* (or *J-V*) *curves*, provide information about the quality of the p-n junction and losses due to resistive components of the device. By repeating the measurements under illumination the performance of the solar cell can be monitored and values of characteristic parameters can be obtained for their quantitative analysis. Furthermore, I-V measurements as a function of temperature and illuminating conditions constitute a powerful tool for the identification of the electronic transport mechanisms governing the device performance.

The I(V, T) analysis typically considers the solar cell under study as an electronic device, being modelled by an equivalent electric circuit with a number of linear (typically resistances) and non-linear (diodes, current sources) components. The complexity of the equivalent circuit designed for modelling a given device will depend on its performance, but the design will always pretend a maximum simplicity, i.e. it will include the minimum number of required components accounting for the device performance. Conventional solid-state-based solar cells are commonly fitted with single- or double-diode equivalent circuits, accounting for the electronic transport processes taking place in parallel during the device performance. Single diode models are routinely used for the characterisation of chalcopyrite-based solar cells (see Refs. [94, 95] and references therein). A typical single-diode equivalent circuit used to simulate the performance of a CGSe-based thin-film solar cell is shown in Figure 10. It includes:

- a diode, which models the p-n heterojunction between the absorber layer and the buffer-window system. The diode is characterised by its ideality factor A and its saturation current J_0, which will determine the diode current J_D flowing through it as a function of the applied voltage.
- a current source, which accounts for the light-generated current J_L. In a first approximation J_L is considered to be bias independent. However, as it will be discussed below, this is normally not the case in thin-film solar cells, and in general $J_L = J_L(V)$. This element is absent in the analysis of dark I-V curves.
- a series resistance R_s, expressed either in [Ω] or in [Ωcm^2] depending on whether considering current I [A] or current density J[Acm^{-2}] in the analysis, which includes a number of resistive effects on the electronic transport, like the contact resistance between the probes and the sample at the front and back contacts and the intrinsic resistivity of the different semiconducting layers making up the device.
- a parallel resistance R_{sh}, expressed either in [Ω] or in [Ωcm^2] as above, also referred to as shunt resistance, which accounts for all possible alternative electronic paths to that of the diode branch for charge transport, e. g. shunts along grain boundaries or lateral currents at the sample edges, resulting in effective electronic losses.

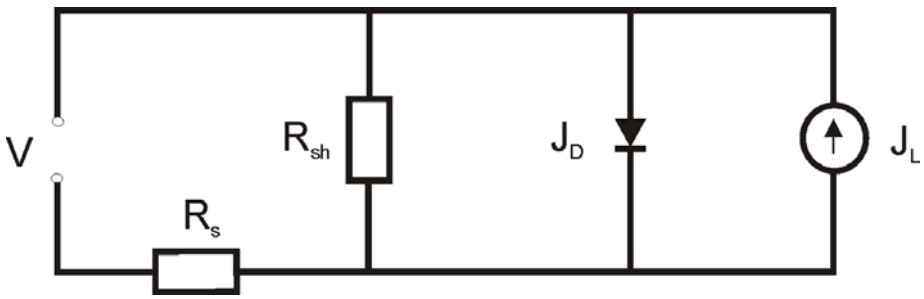

Figure 10. Equivalent circuit based on a single diode model of a CGSe-based thin film solar cell. The current-voltage characteristic can be described in terms of a diode (the p-n heterojunction) through which a current J_D flows, a current source accounting for the light-generated current J_L, and two resistive elements, the series R_s and the parallel (shunt) R_{sh} resistances.

Additional elements may be introduced *a posteriori* in the equivalent circuit if necessary, but the starting model for I(V,T) analysis will base on the scheme of Figure 10. I(V, T) analysis consists of fitting the experimental data with the circuit elements included in the equivalent circuit, in order to reproduce the characteristic I-V with the right choice of values for the set of parameters considered. These include in the single diode model up to four elements (series and parallel resistance, diode ideality factor and saturation current), and two parameters (temperature and photocurrent) assumed to be constant in a given measurement. The current-voltage equation applicable to the circuit in Figure 10 reads:

$$J = J_0\left(\exp\left(\frac{q(V - R_s J(V))}{AkT}\right) - 1\right) + \frac{V - R_S J(V)}{R_{sh}} - J_L \qquad \text{Eq. 50}$$

where the first term on the right represents the diode current (corrected for a voltage drop due to the series resistance), as in Eq. 25 in the previous Chapter; the second term includes the parallel resistance, and J_L represents the photocurrent. The number and possible temperature- and illumination-dependences of the fitting parameters complicate the fitting procedure. Fortunately, the electronic transport of the device can be related to the parameters included in Eq. 50 in different bias ranges, i.e. different elements of the equivalent circuit dominate the electronic transport as a function of the applied voltage, as schematically shown in Figure 11 for the case of a dark J-V. In general, four regions can be distinguished:

- Region I: the reverse bias range of the I-V curve is controlled in the case of an ideal diode by its saturation current, i.e. by the thermal generation of free carriers, as discussed in Chapter 1. In the real case, however, this range will record the simultaneous contributions of the saturation current and the parallel resistance, as leakage currents may also appear.

- Region II (0<V<0.5 V): in the low range of forward bias the saturation current and the parallel resistance still control the electronic transport, resulting from recombination and leakage currents.

- Region III (0.5<V<0.75 V): the characteristic exponential dependence of the current on the applied voltage according to Eq. 50 predicts a linear range in the semilogarithmic I-V plot when the electronic transport is governed by the main diode. Information on the diode ideality factor can be extracted from this bias range, as it controls the slope of the linear range according to Eq. 50.

- Region IV (V>0.75 V): deviations from an ideal diode I-V are expected for large currents as the effect of series resistance becomes more important. The voltage drop at the series resistance for a given value of R_s increases with the current, following Ohm's law, as does the total power dissipated at resistive elements. Therefore, an increasing forward bias increases in turn the power dissipated in the circuit, not all the voltage dropping at the main diode. This is recorded in the semilogarithmic plot as a deviation from the characteristic linearity of region III.

Figure 12 illustrates the effects on simulated dark I-V characteristics following Eq. 50 (excluding the light generated current), resulting from different values of the parameters included in the single diode model. The actual value of these parameters in real devices will depend on the specific electronic mechanisms governing the charge transport, as it will be discussed in Section 2.2.2.1.

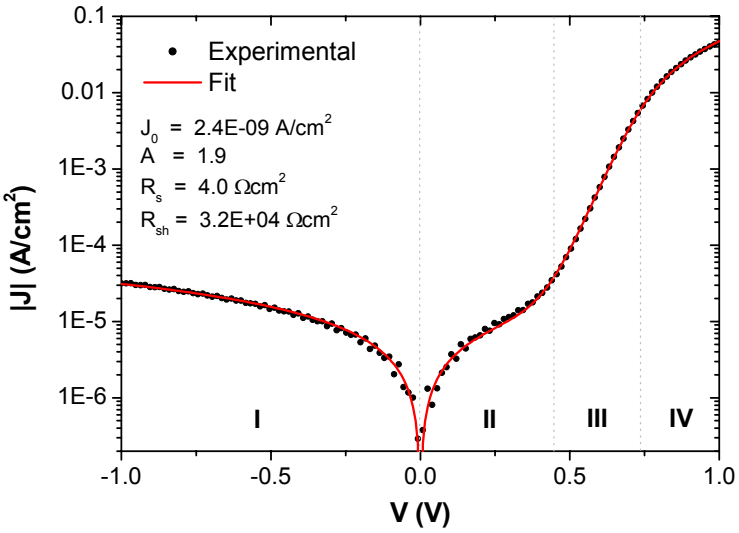

Figure 11. Semi-logarithmic plot of the absolute value of the current density in the dark as a function of the applied bias in a typical CVD-grown CGSe-based thin-film solar cell. Dots correspond to experimental data points, the solid line is the corresponding fit according to Eq. 50 with the given parameter values. Domains I to IV denote the bias range in which different elements of the equivalent circuit control the device electronic transport.

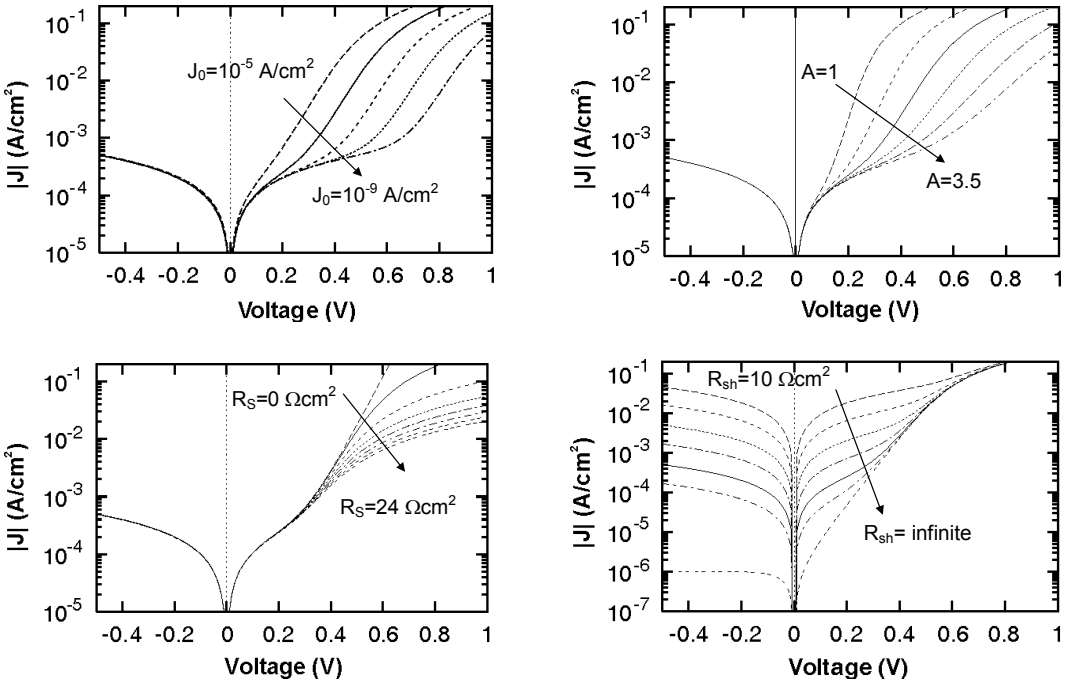

Figure 12. Simulated dark I-V curves obtained from Eq. 50 with varying values of the parameters included in the single diode model, the saturation current J_0 **(upper left)**, ideality factor A **(upper right)**, series resistance R_S **(lower left)** and shunt resistance R_{SH} **(lower right)**. Adapted from Ref [96].

It is thus possible to discern different contributions to the experimental I-V characteristic resulting from different elements of the equivalent circuit. Initial values of

the parallel resistance R_{sh} and saturation current J_0 are determined from the bias range between zero and a few tenths of a volt in forward bias (region II), where Eq. 1 can be simplified neglecting the series resistance and the diode contributions. The initial value of the series resistance R_s can be obtained by fitting in region IV, neglecting in turn the contribution from the shunt resistance. The ideality factor A can be extracted from the slope of the linear range in region III. A non-linear approximation following Eq. 50 is carried then out by the method of least squares X^2, in which the parameters J_0, A, R_s and R_{sh} are varied iteratively until the sum of the weighted difference between the simulated J(V) and the experimental J_i (V) values for all n points considered in a given voltage range is minimum[95], according to:

$$X^2\left(J_0, A, R_s, R_{sh}\right) = \frac{1}{n-4}\sum_i \frac{1}{J_i}\left[J_i - J\left(U_i; J_0, A, R_s, R_{sh}\right)\right]^2 \qquad \text{Eq. 51}$$

The least squares method is reported to provide the best parameter fit for the case of dark I-V curves[97]. By repeating the procedure for every temperature, A(T), $J_0(T)$, $R_s(T)$ and $R_{sh}(T)$ can be determined.

The analysis of illuminated I-V curves can in principle be carried out in the same way as in the case of dark I-V curves, by simply including the constant term J_L in Eq. 50, which accounts for the photogenerated current. This implicitly assumes the validity of the superposition principle, by which photogenerated carriers are effectively collected by the junction, regardless of its biasing conditions. This statement is ultimately incorrect, as the biasing voltage applied to the device will in turn modify the space-charge region width w at the junction, as stated in Eq. 12, and therefore will limit how far electron-hole pairs can be generated in the bulk of the absorber film in order to reach the space-charge region (SCR) and be collected by the junction before they recombine back. Assuming that free carriers in the SCR are swept by the electric field without recombination, this limit is given by the effective diffusion length, defined as:

$$L_{eff}(V) = w(V) + L \qquad \text{Eq. 52}$$

where w denotes the SCR width and L the diffusion length of minority carriers. Only in the case of extremely large values of L, where $L_{eff} \sim L$, can the superposition principle be called valid in first approximation, as the modulation of w with V following Eq. 12 does not affect L_{eff} to a large extent. This is definitely not the case in thin-film solar cells, where the SCR width and the diffusion length show values within the same order of magnitude. A direct analysis of the illuminated I-V according to Eq. 50 would therefore lead to erroneous parameter values if the bias dependence of the photogenerated current is not fully accounted for. A way of circumventing this problem includes the measurement of illuminated I-V curves under different light intensities. At open-circuit, Eq. 50 reads:

$$J_{sc} = J_0\left(\exp\left(\frac{qV_{oc}}{AkT}\right) - 1\right) + \frac{V_{oc}}{R_{sh}} \qquad \text{Eq. 53}$$

assuming $J_L = J_{sc}$, which provides a direct relationship between the short-circuit current and the open-circuit voltage of the solar cell. Different illumination intensities for a

given temperature provide different data points fulfilling Eq. 53. The key point is that Eq. 53 preserves the qualitative J(V) dependence of the dark J-V, i.e. the fitting procedure remains valid and a possible change under illumination of the electronic transport mechanism governing the device performance will be recorded as a change in J_0 and A compared to the values recorded from the dark J-V curves. As an example, Figure 13 shows a J_{sc} vs. V_{oc} plot of a CVD-grown CGSe-based thin-film solar cell measured from 200 to 330 K under different illumination intensities I_{il} by means of a set of neutral filters, from I_{il}=1 (corresponding to standard conditions AM1.5G, as explained later) down to I_{il}=0.00005.

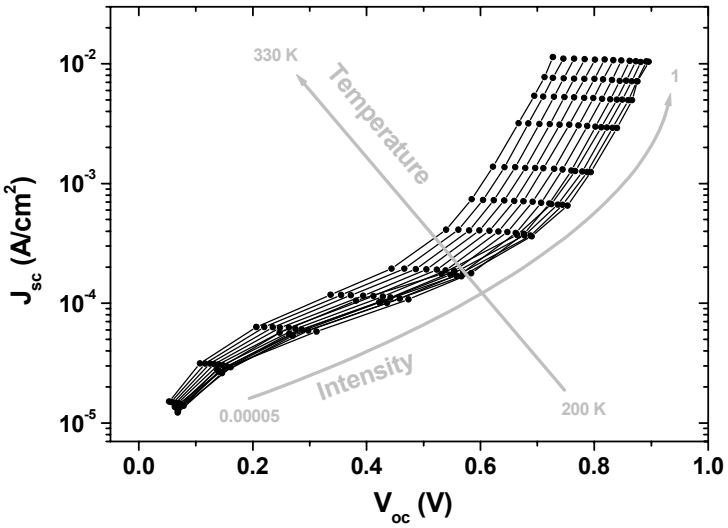

Figure 13. Semilogarithmic plot of experimental short-circuit current vs. open-circuit voltage characteristics of a thin-film solar cell based on CGSe for different values of temperature and light intensity.

The J_{sc}-V_{oc} plot resembles that of the dark I-V in Figure 11 in regions II and III, i.e. the forward bias range excluding the effect of series resistance, explicitly eliminated in Eq. 53 at open-circuit conditions. In this work, the standard analysis of illuminated J-V curves will thus refer to the corresponding J_{sc}-V_{oc} analysis.

2.2.2.1 Recombination mechanisms in thin-film solar cells

As long as the diffusion length of photogenerated minority carriers is shorter than the characteristic dimensions of the semiconductor layers forming the device, recombination mechanisms will control the electronic transport of the solar cell under forward bias. Different processes, as shown in Figure 14, may contribute to an overall recombination rate R, which will account for the total recombination current. Their impact on the device performance is of major importance in device diagnosis, as these recombination mechanisms determine to a large extent the characteristic diode parameters and therefore the ultimate values of its photovoltaic performance. Of critical importance is the role of the heterojunction interface as a drain for charge carriers, due to the high density of electronically active defects resulting from the lattice mismatch

between dissimilar compounds brought into contact. Interface recombination has a direct effect on obtainable open-circuit voltages, and must thus be minimised in order to achieve high efficiency devices[98]. In the following, the main recombination mechanisms expected to operate in the devices under study will be reviewed, with particular attention to those aspects that may help discerning between them.

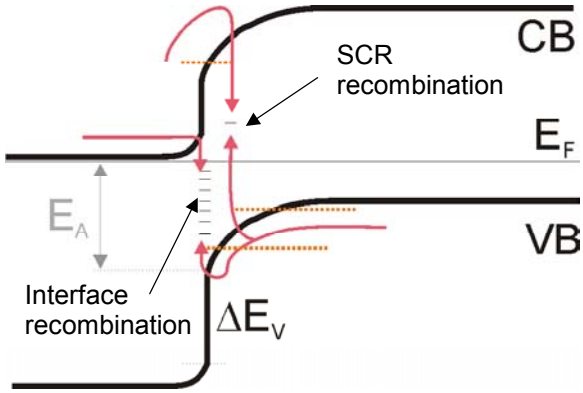

Figure 14. Main recombination mechanisms of charge carriers in a heterojunction-based device with a valence band offset ΔE_V. E_F is the Fermi level in equilibrium, CB and VB the conduction and valence bands, respectively. Recombination may occur via defect states within the band gap, situated either in the bulk (SCR) of the absorber layer or at the interface between the absorber and window materials. Solid lines indicate thermally activated processes, whereas dotted lines denote tunnelling enhancement.

Generally speaking, the total recombination current can be expressed as:

$$J = q\int R dx \qquad \text{Eq. 54}$$

where R denotes the recombination rate of electron-hole pairs and the integral extends over the region where recombination events take place (e.g. the SCR, or the entire absorber layer). A generalised analytical expression for the recombination rate R was given by Rau[99], based on the classical Shockley-Read-Hall (SRH) model[100,101] of bulk recombination via a discrete defect level in the band gap, and the work of Hurkx *et al.*[102], including tunnelling-assisted recombination, which reads:

$$R = \frac{np - n_i^2}{\gamma_p (n + n^*) + \gamma_n (p + p^*)} \qquad \text{Eq. 55}$$

where n_i denotes the intrinsic carrier concentration for a given temperature, $n^*=N_C\exp[(E_T-E_C)/kT]$ and $p^*=N_V\exp[(E_V-E_T/kT)]$ denote the electron and hole concentrations obtained if the Fermi level lied at the defect level E_T, and $\gamma_{n,p}$ include corrections due to tunnelling processes. Eq. 55 can be used to describe interface

recombination, as well as bulk recombination via trap states. In the case of interface recombination R is given in units of $cm^{-2}s^{-1}$, and $\gamma_{n,p}$ are defined according to:

$$\gamma_{n,p} = \frac{1}{S_{n,p}(1+\Gamma)} \qquad \text{Eq. 56}$$

where $S_{n,p}$ denote the interface recombination of electrons and holes, as explained later, and Γ is the correction factor describing the recombination enhancement due to tunnelling assisted processes. In the case of bulk recombination, R is expressed in units of $cm^{-3}s^{-1}$ and $\gamma_{n,p}$ are defined according to:

$$\gamma_{n,p} = \frac{\tau_{n,p}}{(1+\Gamma)} \qquad \text{Eq. 57}$$

where $\tau_{n,p}$ denote the lifetimes of electron and holes. Eq. 55 is thus the starting point for the analysis of recombination processes. Following the works of Hengel[94] and Reiss[95], it will be shown that the theoretical models developed for the different recombination mechanisms predict particular relationships between the diode parameters, including temperature dependencies, as summarised at the end of the section in Table 1, that will be used in Chapter 4 to identify experimentally those processes controlling the device performance.

- Recombination in the SCR: thermally activated processes.
  According to Eq. 55, the driving parameter of the recombination rate is the difference in carrier concentration between the product np and n_i^2 (i.e. the excess carrier concentration induced e.g. by illuminating the semiconductor film). According to the general theory of semiconductors (see for instance Ref. [57]) the following expression holds within the entire semiconductor between majority and minority carrier concentrations, for given biasing conditions:

  $$np = n_i^2 \exp\left(\frac{qV}{kT}\right) \qquad \text{Eq. 58}$$

  Substituting this expression in Eq. 55, and assuming[h] that $\gamma_n=\gamma_p$, it follows that the recombination rate is maximum when n+p is minimum, which is the case for n=p. Excluding for the moment the participation of tunnelling events in the recombination (i.e. setting Γ=0 in Eq. 57), Eq. 55 leads to:

  $$R_{\max} = \frac{n_i}{2\tau}\left(\exp\frac{qV}{kT} - 1\right) \qquad \text{Eq. 59}$$

  the recombination being effective in the region $\delta x \sim 2kT/qE_{max}$ (where E_{max} denotes the maximum electric field) around the position where p=n. If δx does

[h] Equivalently, equal capture cross sections are assumed for electrons and holes, which is a reasonable statement following the SRH theory for defects lying at mid-gap.

not depend strongly on the applied bias, the recombination current (Eq. 54) can be approximated by:

$$J = qR_{\max}\delta x \approx \frac{qn_i}{2\tau}\delta x\left(\exp\frac{qV}{2kT}-1\right) = J_0\left(\exp\frac{qV}{2kT}-1\right) \qquad \text{Eq. 60}$$

This expression resembles that derived for the diode in Eq. 25, predicting an ideality factor A=2 for the case in which the electronic transport in the device is controlled by carrier recombination taking place in the SCR, without tunnelling enhancement, and via a single defect level in the band gap of the absorber film. The corresponding saturation current can be written as:

$$J_0 = J_{00}\exp\left(\frac{-E_g}{2kT}\right) \qquad \text{Eq. 61}$$

which states that the saturation current of such device is thermally activated, with an activation energy $E_A=E_g/2$. Substituting this expression in Eq. 60, and neglecting the effect of a finite shunt resistance, a relationship between the open-circuit voltage and the short-circuit current can be obtained:

$$qV_{OC} = E_g - 2kT\ln\left(\frac{J_{00}}{J_{SC}}\right) \qquad \text{Eq. 62}$$

According to this expression, the extrapolation to T=0 K of V_{OC} as a function of the temperature should yield the energy band gap of the absorber.

The model of thermally activated recombination within the SCR was extended by Walter *et al.*[103] from the simple case based on the SRH theory of a single defect level in the band gap, to a continuous defect density distribution $N_T(E)$ from the band edges decaying into the gap according to an exponential function:

$$N_T = N_{T0}\exp\left(-\frac{E_C - E}{kT^*}\right) \qquad \text{Eq. 63}$$

where kT^* is the characteristic energy of the exponential decay. The defect distribution N_T can be introduced in Eq. 55 via the carrier lifetime, which can in turn be expressed as:

$$\tau = \sigma v_{th} N_T \qquad \text{Eq. 64}$$

Here, σ denotes the carrier capture cross section of the defect and v_{th} is the thermal velocity of the free carriers. Substituting in Eq. 55, it follows that R is maximum for $T^*>T$ at the point where n=p, which indeed states that the recombination takes place in the energy range comprised between the quasi-Fermi levels[103] under applied bias. The ideality factor of a device controlled by

recombination over a distribution of defect states is slightly temperature dependent, according to the expression:

$$A = 2\frac{T^*}{T + T^*} \qquad \text{Eq. 65}$$

which predicts increasing values of the ideality factor between 1 and 2 with decreasing temperatures. The saturation current is thermally activated with $E_A=E_g/A$, following:

$$J_0 = J_{00}\exp\left(-\frac{E_g}{AkT}\right) \qquad \text{Eq. 66}$$

and the J_{SC}-V_{OC} dependence reads:

$$qV_{OC} = E_g - AkT\ln\left(\frac{J_{00}}{J_{SC}}\right) \qquad \text{Eq. 67}$$

Thus, the extrapolation to T=0 K of the open-circuit voltage as a function of temperature should also give, in the case of energetically distributed defects, a value corresponding to the band gap of the absorber.

- Recombination in the SCR: Tunneling enhancement.
  The model of tunnelling enhanced recombination over a continuous defect distribution within the SCR of the type given by Eq. 63 predicts a temperature dependence of the ideality factor given by[99]:

$$\frac{1}{A} = \frac{1}{2}\left(1 - \frac{E_{00}^2}{3(kT)^2} + \frac{T}{T^*}\right) \qquad \text{Eq. 68}$$

for $kT>E_{00}$, where E_{00} is the characteristic energy of the transition from tunnelling to thermally activated processes, and kT^* is the characteristic energy of the defect distribution. The saturation current reads in this case:

$$J_0 = J_{00}\exp\left(-\frac{E_g}{AkT}\right) \qquad \text{Eq. 69}$$

and the J_{SC}-V_{OC} relationship predicts:

$$qV_{OC} = E_g - AkT\ln\left(\frac{J_{00}}{J_{SC}}\right) \qquad \text{Eq. 70}$$

analogously to the case of thermally activated recombination.

- Recombination at the interface: thermally activated processes.
  A phenomenological description of surface and interface recombination was proposed by Stevenson and Keyes[104], which can be interpreted in terms of a surface recombination velocity S, as pointed out in Eq. 56. This parameter is defined as the number of carriers recombining at the surface per unit area per unit time per unit volume of excess bulk carriers at the boundary between the quasi-neutral region and the depletion region associated to the surface. The surface recombination velocity is proportional to the surface density of states and its value will be limited by the velocity with which carries arrive to the surface (ideally, the thermal velocity in absence of surface band bending; in practice, the drift velocity associated to the surface potential). Each recombination centre is characterised by its capture cross section of electrons and holes, the smaller of which acts as a bottle neck, determining the effectiveness of the given trap as a recombination centre or simply as a trapping centre. Those centres whose energy levels are located between the Fermi level at the surface and mid gap are most effective in recombination, with S at its maximum value when the Fermi level is pinned at midgap.

  In this type of recombination, the rate strongly depends on the doping concentrations on either side of the interface. Furthermore, the ideality factor of a p-n junction governed by interface recombination explicitly depends on the net doping ratio, which for the case of materials with identical dielectric constants on either side of the interface can be approximated by (see Ref. [61]):

$$A = 1 + \frac{N_A}{N_D} \qquad \text{Eq. 71}$$

  From this, an ideality factor of 2 is expected for the case of $N_A=N_D$, whereas A=1 is expected for the case of a high-low junction (e.g. for $N_D>>N_A$). The recombination current due to interface states at the heterojunction can be derived from simple considerations based on Figure 14. The potential barrier that holes must surmount in order to reach the interface and recombine with electrons from the window is given by E_A, determined by the energy difference between the hole quasi-Fermi level and the valence band edge on the absorber side of the interface. Assuming that this potential barrier does not depend on the applied bias, the recombination current can be written from Eqs. 54 and 55 as:

$$J = q\gamma_n N_V \left(\exp\left(\frac{qV}{kT}\right) \exp\left(-\frac{E_A}{kT}\right) \right) = J_{00} \exp\left(\frac{-E_A}{kT}\right) \exp\left(\frac{qV}{kT}\right) \qquad \text{Eq. 72}$$

  An ideality factor A=1 is predicted, and the J_{SC}-V_{OC} dependence reads:

$$qV_{OC} = E_A - kT \ln\left(\frac{J_{00}}{J_{SC}}\right) \qquad \text{Eq. 73}$$

The extrapolation to T=0 K of the open-circuit voltage yields the activation energy of the interface recombination process E_A, as defined above.

- Recombination at the interface: tunnelling enhancement.
  The inclusion of tunnelling events participating in the interface recombination can be conducted again by means of Eq. 56, leading to a general expression of the recombination current given by:

$$J = J_{00} \exp\left(\frac{-E_A}{AkT}\right)\exp\left(\frac{qV}{AkT}\right) \qquad \text{Eq. 74}$$

which states, as in the case of thermally activated interface recombination, that the activation energy of the saturation current is given by E_A. The ideality factor in this case is explicitly temperature-dependent, following:

$$A = \frac{E_{00}}{kT}\coth\left(\frac{E_{00}}{kT}\right) \qquad \text{Eq. 75}$$

where E_{00} has the same meaning as in the case of tunnelling enhanced SCR recombination. The open-circuit voltage reads:

$$qV_{OC} = E_A - AkT\ln\left(\frac{J_{00}}{J_{SC}}\right) \qquad \text{Eq. 76}$$

From the above considerations it is clear that the Fermi level position at the heterojunction interface plays a key role in establishing what kind of recombination mechanism controls the transport and where it is most likely to occur. According to the model of Shockley and Read[100] and Hall[101], the recombination is most effective in the vicinity of the position where the electron and hole concentrations are equal, n=p. In the case of a p-n heterojunction, like in CGSe-based thin film solar cells, this is expected to occur directly at the heteointerface between the p-type CGSe and the n-type CdS, unless the induced band bending resulting from the junction formation is large enough to shift the Fermi level in the absorber from mid gap closer to the conduction band edge at the junction, leading to a type inversion of the absorber in the near interface region. In the case of surface inversion, the electronic p-n junction is located within the absorber layer, reducing the probability of surface recombination events at the expense of increasing the recombination in the bulk. As the interface is typically a highly defective region, and the recombination rate shows in turn a linear dependence on the defect density through which the recombination takes place, the surface inversion invariably leads to an improved device performance, reducing losses in open-circuit voltage and yielding higher values of the fill factor. The eventual type inversion of CGSe in heterojunction devices is still controversial[105], whereas it is well accepted[95] for related materials like $Cu(In,Ga)Se_2$ and $CuInSe_2$, being a fundamental *must* for the outstanding performance of such devices.

Table 1 summarises the different recombination mechanisms considered above and the corresponding activation energies of the saturation current, extrapolated values down to

T=0 K of the open-circuit voltage, and the temperature dependence of the ideality factor. In real devices, one or more of these recombination mechanisms may dominate the electronic transport. Furthermore, changes can be recorded as a function of illumination or at different temperature ranges in the recombination mechanisms. In general, the total recombination current will be given by the sum of the different contributions resulting from the corresponding recombination processes, which can be written as :

$$J = \sum_i J_{0i}\left(\exp\left(\frac{qV}{A_i kT}\right) - 1\right) \qquad \text{Eq. 77}$$

where i runs over the recombination processes involved in the transport. In principle, these can be identified from the analysis of the I-V characteristics at different temperatures and from the temperature dependences of the diode parameters. This task will be addressed in Chapter 4, where the limiting recombination mechanisms of CGSe-based devices will be evaluated.

Table 1. Summary of recombination mechanisms expected to participate in the electronic transport of CGSe-based thin-film solar cells. Activation energies of the saturation current J_0, extrapolated values down to T=0 K of the open-circuit voltage and temperature dependences of the ideality factor A are included. Adapted from[94,95].

Recombination mechanism	Activation energy of J_0	V_{OC} (T=0 K)	Ideality factor A
Bulk	E_g	E_g	1
Thermally activated SCR-single defect level	E_g	E_g	2
Thermally activated SCR-exponential defect distribution	E_g/A	E_g	$\frac{2T^*}{T+T^*}$; 1≤A≤2
Tunneling enhanced SCR	E_g/A	E_g	$2\left(1-\frac{E_{00}^2}{3(kT)^2}+\frac{T}{T^*}\right)^{-1}$; A↑ as T↓
Thermally activated interface	$E_A<E_g$	E_A	$1+\frac{N_A}{N_D}$; 1≤A≤2
Tunneling enhanced interface	$E_A<E_g$	E_A	$\frac{E_{00}}{kT}\coth\left(\frac{E_{00}}{kT}\right)$; A↑ as T↓

In order to perform reproducible measurements of illuminated I-V curves, standards have been adopted for laboratory illumination conditions simulating the sunlight. The standards are characterised by the so-called *air mass* (AM), equivalently the optical path of the real sun light when crossing the terrestrial atmosphere before reaching the sample, and the kind of radiation incidence impinging on the sample, either direct (D)

or global (G, including scattered light). This work will only refer to the standard AM1.5G spectrum. Further details and numerical values can be found in Ref. [65].

I-V measurements have been performed in the frame of this work in two different set-ups, whose main features are briefly reviewed in the following.

- Sun simulator.
  AM1.5G illumination conditions are simulated by combining a 100 W Xenon lamp and a 120 W halogen lamp in order to cover the sunlight spectrum, as shown in Figure 15. The system is periodically calibrated with a Si-reference solar cell. Slight differences in the spectral content of the lamps and the AM1.5G reference spectrum are compensated to yield the same short-circuit current in the reference cell by adjusting the lamp positions. I-V measurements are performed in the four-probe configuration to minimise effects associated to the contact resistance, with two pairs of needle probes, one on the rear contact and another on the Ni-Al front contact of the devices, which are connected to the measuring unit (Keithley SMU 238). The unit generates the voltage and measures the corresponding current, as specified in the computer, where collected data are stored. A thermostat keeps the temperature of the sample holder at a given value, normally set at 23 °C for standard measurements.

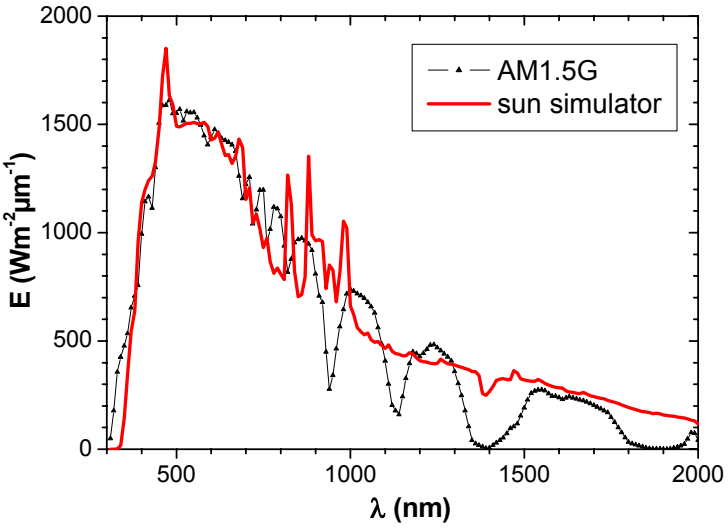

Figure 15. Spectral content of the standard AM1.5G (after Ref. [65]) and the sun simulator illumination source used in this work.

- I(V, T) set up.
  The experimental set up is shown schematically in Figure 16 and consists of a sample holder mounted in a cryostat, the latter provided with a quartz window allowing illumination. The sample holder is a hollow piece of steel, which is flooded with liquid nitrogen for refrigeration. The cryostat in turn is evacuated with a turbo-pump once the sample has been mounted. The typical temperature range for the analysis extends from 150 K to 350 K in steps of 10 K, controlled by a thermocouple, and governed by an electrical heater. Illuminated I-V

curves can be recorded for different illumination intensities I_{il} ($0.00005<I_{il}<1$, with $I_{il}=1$ being approximately the AM1.5G reference) by means of a neutral filter wheel located between the lamp and the cryostat quartz window. The sample is contacted in the four-point-probe configuration, as in the case of the sun simulator. The measuring unit (Keithley SMU 238) generates the voltage and measures the corresponding current. The system is completed with a single halogen lamp as illumination source and a shutter for switching from dark to illuminated measuring conditions. Differences in the spectral content of the illumination source are thus introduced relative to the measurements performed in the sun simulator, in particular a reduction of the blue content, which is of minimal relevance for this study. This mismatch is compensated by adjusting the short-circuit current as measured in the I(V, T) set up to the value obtained previously in the sun simulator, in order to ensure the same amount of current flowing through the device as in standard conditions. Nevertheless, absolute values of PV parameters (V_{oc}, J_{sc} and FF) as recorded in the I(V, T) set up are only approximate, and their full meaning must be evaluated in a relative scale when comparing measurements under different illumination conditions.

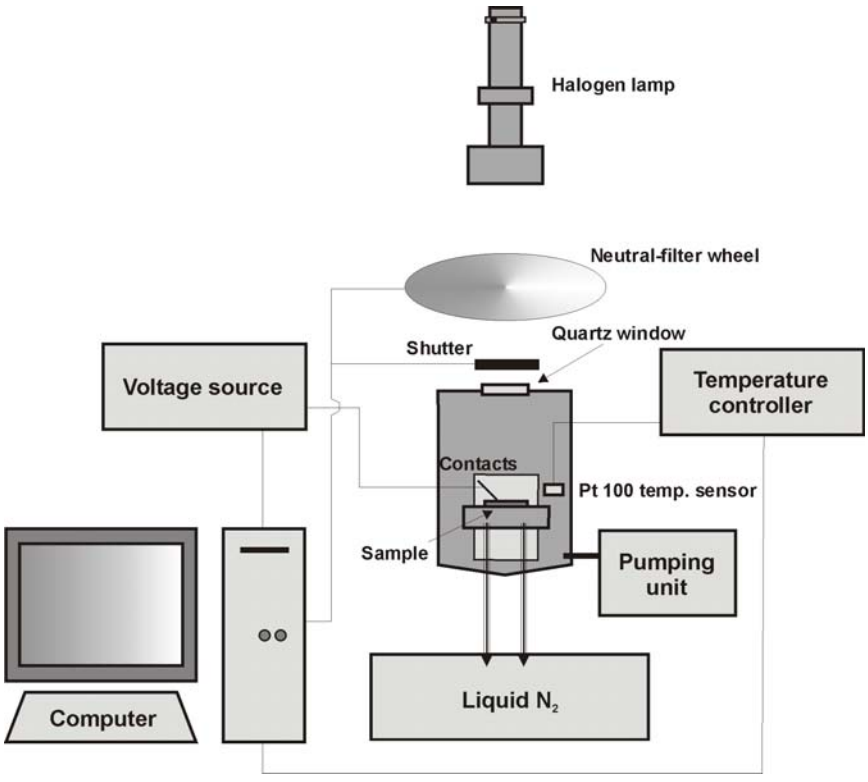

Figure 16. Schematic overview of the I(V, T) set up used in this work. The sample is located in an evacuated cryostat with a quartz window on the top side. Illumination is provided by a halogen lamp. A shutter above the quartz window permits measurement in darkness and under illumination. The temperature of a given measurement is regulated with a temperature controller and a controlled flow of liquid nitrogen. A filter wheel with 12 neutral density filters allows to measure I-V curves under different illumination intensities.

2.2.3 Quantum efficiency (QE)

The quantum efficiency (QE) of a solar cell is defined as the ratio of outgoing electrons to incoming photons under given working conditions, which may be a function of the temperature, the spectral content of the illumination source and the applied voltage. It is perhaps the most characteristic parameter of a solar cell, as it provides a direct measurement of the performance for which it was designed for, the transformation of light into electricity. Ideally, a device would show QE values of unity independently of the wavelength of the impinging photons. This would in turn mean that every photon, regardless of its energy, falling on the device generates an electron-hole pair which is effectively separated by the electric field present at the p-n junction. This is not a realistic situation, and a number of factors listed in the following and summarised in Figure 17 bring this number down from unity in all real cases:

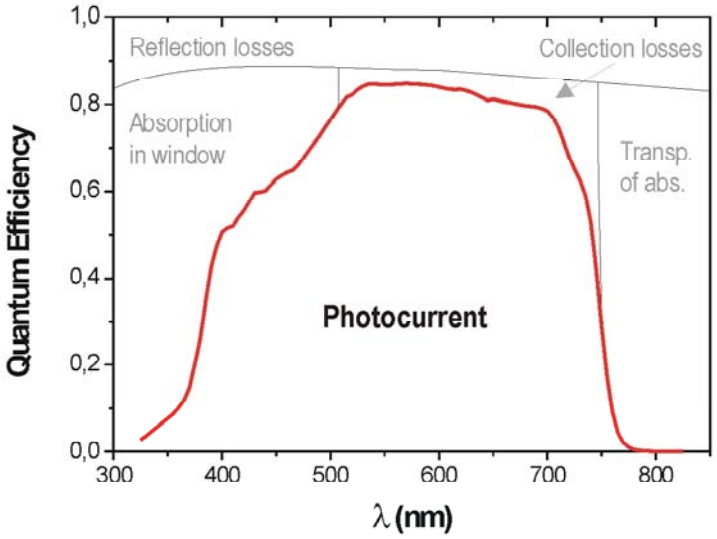

Figure 17. Quantum efficiency of a CVD-grown CGSe-based thin-film solar cell at room temperature and zero bias. The region below the curve accounts for the photocurrent the device can supply under short-circuit conditions. Different types of losses are schematically shown, which reduce the device output.

- A minimum photon energy is necessary in order to generate charge carriers in the absorber layer, this energy being related to the energy gap of the material. Even though excitation of charge carriers may occur with photon excitation energies below the gap (e. g. in transitions starting from or ending at defect states within the gap, or in the so-called two-step excitation[106]), these events do generally not end up with mobile free charge carriers in the valence or conduction bands, or their probability of occurrence is several orders of magnitude lower than band-to-band transitions, or both, and most of the low energy photons either simply pass across the material not interacting with it or inducing different kind of interactions (e.g. excitation of vibrational modes in

the infrared range, free carrier reflectivity in the microwave range, among others) not related to electronic transitions in the optical range. This means that for practical purposes, only photons with energies larger than the absorber band gap will contribute to the photocurrent, the rest being lost for its conversion into electricity due to the transparency of the absorber.

- Not even all photons with energy enough to generate charge pairs do so, as some of them are reflected at the device top surface. Reflectance is a wavelength-dependent property of a given material. Antireflection coatings, which minimise the reflectivity of a given material for certain wavelengths, and surface texturing of the material surface, which increases the probability of light absorption by multiplying the number of reflections a given photon may undergo when impinging the material, can effectively reduce this loss of raw material for the photovoltaic application. The reflectance of a typical CGSe-based thin-film solar cell, based on the layered structure given in Section 1.3, is shown in Figure 18, accounting about 5 to 7 % in the useful wavelength range. Metal grids providing front contacts to the device constitute an unavoidable reflection source. This shading effect is minimised with finger-like design of the front contact pattern, as mentioned in Chapter 1, in a trade-off between shadowing on one hand and charge collection and resistivity on the other hand.

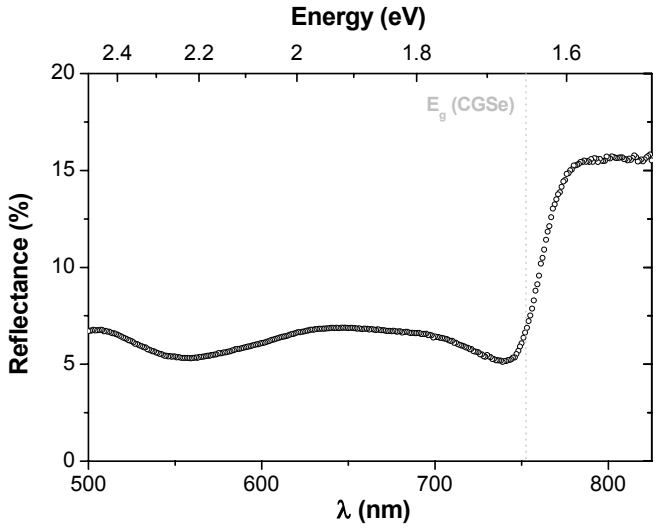

Figure 18. Reflectance of a CVD-grown CGSe solar cell (without metal grid). The dotted line indicates the band gap of the CGSe absorber layer.

- Additional losses occur in processes which do generate electron-hole pairs but whose separation is afterwards not successful. This can be the result of absorbing photons in the window and buffer layers, regions where minority carriers posses extremely brief lifetimes, due to a high doping concentration and/or a high density of defects and recombination centres. A non-effective charge separation can also happen for charge pairs which have been generated within the absorber layer if the diffusion length of the minority carriers is low, resulting in recombination processes that eventually can re-emit the photon back, like in photoluminescence. Losses related with the absorption in the window and buffer layers are associated to a significant decrease of the QE for

photon energies higher than the band gap of the corresponding materials, whereas collection losses in the absorber layer result in lower QE values in the long wavelength range.

From Figure 17 it is clear that the quantum efficiency is a function of the photon wavelength, as this parameter will determine with which probability the photon will be either reflected or transmitted, and with which probability the photon will be absorbed either in the window or within the absorber layer. Furthermore, in the latter case the position at which the actual electron-hole pair generation occurs, and thus the likelihood that the minority carrier can manage to reach the p-n junction via its diffusion length, do also depend on the incoming photon wavelength, as result of the characteristic penetration depth of a given photon as a function of its energy.

Additionally, the application of external voltage bias alters the electric field and the space charge region width associated to the junction, resulting in a bias-dependence of the quantum efficiency that superimposes to that related to the photon wavelength, as shown in Figure 19. The enlargement of the depletion region under reverse bias according to Eq. 25 results in an enhancement of the carrier collection. On the contrary, a forward bias reduces the width of the space-charge region, reducing the quantum efficiency yield. The application of an external voltage bias also affects the distribution of charge at the interfaces (heterojunctions and grain boundaries), as well as the concentration of charge carriers localised at deep trapping centres within the absorber bulk. The different contributions accounting for the complete bias dependence of the QE can in principle be separated in analytical expressions, if some assumptions are made, as explained in the following.

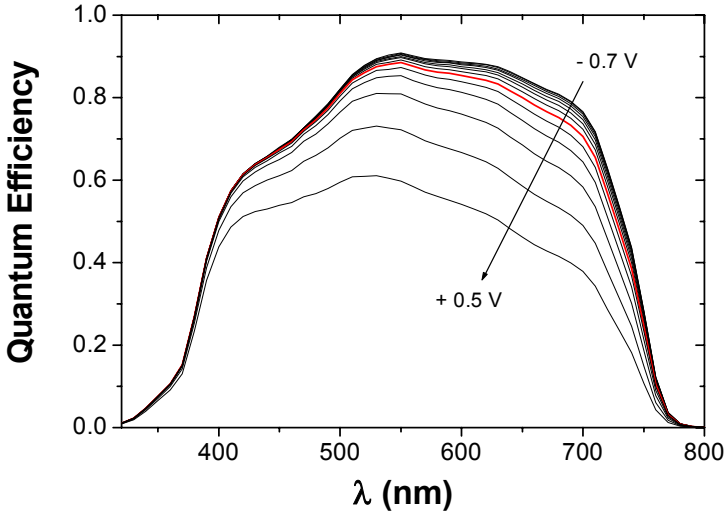

Figure 19. Quantum efficiency of a CVD-grown CGSe-based thin-film solar cell at room temperature under different biasing conditions, from 0.7 V in reverse bias to 0.5 V in forward bias in steps of 0.1 V.

The quantum efficiency of a device is in practice measured by illuminating the sample with a light source of known specifications and spectral content and measuring the

current flowing through the device in steady state conditions. The so called *external* quantum efficiency (EQE) is by definition given by:

$$EQE(\lambda,V) = \frac{j(\lambda,V)}{q\Phi_{ph}(\lambda)} \qquad \text{Eq. 78}$$

where j(λ,V) denotes the electric current density through the diode as a function of the incident light wavelength and bias conditions, and Φ_{ph} is the illuminating photon flux as a function of the incident light wavelength. From Eq. 78, it follows:

$$j(V) = \int EQE(\lambda,V) q\Phi_{ph}(\lambda) d\lambda \qquad \text{Eq. 79}$$

and therefore the current flowing through the device for a given voltage can be obtained from the integration of the photon flux, weighted with the EQE, over the excitation wavelength range. Every voltage value gives therefore one current value, and the corresponding I-V curve can be thus plotted, for a given temperature. The expression for EQE can be corrected accounting for reflection and transmission losses of the layer stack making up the device, resulting in the *internal* quantum efficiency defined as:

$$IQE(\lambda,V) = \frac{EQE(\lambda,V)}{(1-R(\lambda))T(\lambda)} \qquad \text{Eq. 80}$$

An equivalent definition of QE, stressing the two-stage character of the photocurrent generation, can be stated as follows:

$$IQE(\lambda,V) = g(\lambda)F(\lambda,V) \qquad \text{Eq. 81}$$

where g denotes the generation function (i.e. the probability that a given photon of wavelength λ generates an electron-hole pair) and F represents the collection function of the p-n junction (i.e. the probability that a photogenerated minority carrier can be collected by the junction, as discussed in Section 2.2.1). The equivalence between Eqs. 80 and 81 can be explicitly stated from the analytical expressions of g and F. From the Beer-Lambert law of light absorption:

$$\Phi_{ph}(x,\lambda) = \Phi^0_{ph}(\lambda) e^{-\alpha(\lambda)x} \qquad \text{Eq. 82}$$

where Φ^0_{ph} is the photon flux of the incoming light, α is the absorption coefficient and x is the depth at which the photon flux Φ_{ph} is measured inside the sample. From Eq. 82, the fraction of light absorbed up to a depth x in the semiconductor is:

$$\frac{\Phi^0_{ph}(\lambda)}{\Phi^0_{ph}(\lambda) - \Phi_{ph}(x,\lambda)} = 1 - e^{-\alpha(\lambda)x} \qquad \text{Eq. 83}$$

Assuming that each absorbed photon generates an electron-hole pair, the generation function g is then given by:

$$g(x,\lambda) = 1 - e^{-\alpha(\lambda)x} \qquad \text{Eq. 84}$$

The collection function can be calculated following the approach of Gärtner[107]. Assuming that no recombination takes place within the SCR, that minority carrier transport is limited by diffusion in the quasi-neutral region, and neglecting recombination at the rear contact, the photogenerated current can be expressed as the sum of two contributions: those minority carriers generated in the SCR (and thus, automatically collected without losses, according to the first assumption) and those minority carriers generated in the bulk which reach the SCR edge by diffusion:

$$J_{ph} = J_{ph}^{w} + J_{diff} \qquad \text{Eq. 85}$$

Now, from Eqs. 79 and 81-84:

$$J_{ph}^{w}(\lambda) = q\Phi_{ph}^{0}(\lambda)g(w,\lambda) = q\Phi_{ph}^{0}(\lambda)\left(1 - e^{-\alpha(\lambda)w}\right) \qquad \text{Eq. 86}$$

and the diffusion current of minority carriers at the SCR edge w is given by the standard theory from Schockley[59] as:

$$J_{diff}(\lambda) = q\Phi_{ph}^{0}(\lambda)\frac{e^{-\alpha(\lambda)w}}{1 + \frac{1}{\alpha(\lambda)L}} \qquad \text{Eq. 87}$$

where L denotes the diffusion length of the minority carriers. Substituting Eqs. 86 and 87 into Eq. 85, the total photocurrent can be obtained, which in turn can be substituted in the original Eq. 78, including the optical losses by transmission and reflection, resulting in:

$$IQE(\lambda) = 1 - \frac{e^{-\alpha(\lambda)w}}{1 + \alpha(\lambda)L_{diff}} \qquad \text{Eq. 88}$$

Additional corrections to Gärtner's model can be introduced by taking into account photocurrent losses due to interface recombination at the p-n junction, as discussed in the preceding section. The recombination current reads:

$$J_R = J_{ph}\left(\frac{S_n}{S_n + v_{dr}}\right) \qquad \text{Eq. 89}$$

where the term in parentheses accounts for the recombination losses, given by the ratio between the surface recombination velocity S_n and the provision of carriers by the field to recombine at the surface, with the drift velocity v_{dr} given by:

$$v_{dr} = \mu_n E_j \qquad \text{Eq. 90}$$

where μ_n is the mobility of the minority carriers (in this case electrons) and E_j is the magnitude of the electric field at the heterojunction. Subtracting the recombination current from the photocurrent J_{ph}^0 as derived in Eq. 85, results in:

$$J_{ph}(\lambda) = J_{ph}^0 - J_R = q\Phi_0(\lambda)\left(1-\frac{e^{-\alpha(\lambda)w}}{1+\alpha(\lambda)L}\right)\left(1+\frac{S_n}{\mu_n E_j}\right)^{-1} \quad \text{Eq. 91}$$

which can be in turn substituted in the general expression of QE (Eq. 78), leading to:

$$IQE(\lambda) = \left(1-\frac{e^{-\alpha(\lambda)w}}{1+\alpha(\lambda)L}\right)\left(1+\frac{S_n}{\mu_n E_j}\right)^{-1} \quad \text{Eq. 92}$$

This expression fully accounts for the wavelength dependence of the QE and additionally introduces the necessary elements to include the effects of an external voltage bias on the spectral response of the sample under study. Two parameters in Eq. 92 are bias-dependent, namely the SCR width w and the electric field at the junction E_j. For the case of an ideal Schottky contact or a high-low junction with $N_D >> N_A$, where all the potential drop and the corresponding band bending takes place in the absorber, Eqs. 93 and 94 hold:

$$w = \sqrt{\frac{2\varepsilon\varepsilon_0\left(V_{bi}-V_{app}\right)}{qN_A}} \quad \text{Eq. 93}$$

$$E_j = \sqrt{\frac{2qN_A\left(V_{bi}-V_{app}\right)}{\varepsilon\varepsilon_0}} \quad \text{Eq. 94}$$

where $\varepsilon\varepsilon_0$ is the dielectric constant of the absorber, V_{bi} the built-in potential of the heterojunction, and V_{app} the external applied bias. From Eq. 92 it follows that a change in biasing conditions will revert simultaneously in a change of the total interfacial charge stored at the junction (altering the conditions for surface recombination and therefore the recombination current at the interface) and the subsequent readjustment of the band bending within the SCR to account for changes in the electric field. In other words, the actual SCR width w will include the effect of the interfacial charge present at the junction, as the interfacial charge must be compensated with a change in the net charge in the bulk of the SCR, in order to ensure the condition of charge neutrality. Furthermore, Eqs. 93 and 94 assume that the entire SCR is located within the absorber layer, an assumption that must be corrected to fully account for interfacial issues related to the presence of the buffer layer in actual heterojunctions. Nevertheless, it is the charge neutrality statement that allows, in principle to separate analytically the contributions from bulk and interface charge to the total absorber SCR width, according to the expression derived by Rau[108] for n^+-ZnO/buffer/p-absorber:

$$Q_n + qd_bN_b - Q_i - qwN_A = 0 \quad \text{Eq. 95}$$

where Q_n denotes the window layer charge (due to ionised donors), assumed to be located at the surface due to its high doping concentration; Q_i denotes the charge density stored at interface states between the absorber and buffer layers; N_A and N_b denote respectively the absorber (acceptor) and buffer (donor) net doping concentrations, w is the SCR width in the absorber and d_b the thickness of the buffer layer, assumed to be depleted of free carriers. The charge neutrality statement must explicitly include the band offsets originated at each heterointerface. These, and the general band diagram of the heterostructure, are schematically shown in Figure 3. The potential drop in the buffer layer is given by:

$$qV_{bi}^{CdS} = \frac{Q_n d_b}{\varepsilon\varepsilon_0} + \frac{qN_b d_b^2}{2\varepsilon\varepsilon_0} \qquad \text{Eq. 96}$$

From the window side, the conduction band alignment follows:

$$\Delta E_{C1} + qV_{bi}^{CdS} - \Delta E_F + \Delta E_{C2} = 0 \qquad \text{Eq. 97}$$

where $\Delta E_{C1,2}$ denote the band offsets at the window/buffer and buffer/absorber interfaces, and ΔE_F represents the energy difference between the Fermi level and the absorber conduction band edge at the absorber/buffer interface. From the absorber side:

$$E_g^{abs} - \frac{qN_A w^2}{2\varepsilon\varepsilon_0} - \xi - \Delta E_F = 0 \qquad \text{Eq. 98}$$

must hold, where the second term denotes the potential drop qV_{bi}^{CGSe} within the absorber SCR, E_g^{abs} is the energy band-gap of the CGSe absorber, N_A its net aceeptor concentration and ξ is the energy difference between the Fermi level and the valence band edge in the quasi-neutral region. Equating the last two expressions, and substituting Q_n and qV_{bi}^{CdS} from Eqs. 95 and 96, an explicit expression for the SCR width, correcting that given in Eq. 25, is obtained as a function of the applied bias:

$$w(V) = -d_b + \sqrt{d_b^2 + \frac{2\varepsilon\varepsilon_0}{qN_A}\left(E_g - \Delta E_C - \xi - \frac{Q_i d_b}{\varepsilon\varepsilon_0} + \frac{qd_b^2 N_b}{2\varepsilon\varepsilon_0} - qV\right)} \qquad \text{Eq. 99}$$

where the same value of the dielectric constant for both buffer and absorber layers has been considered. Eq. 99 explicitly states the dependence of the SCR width with the buffer thickness, as the buffer layer was assumed to be depleted of free carriers. Furthermore, it is evident from the term in brackets that the potential drops not only as a function of the position of the Fermi level in the SCR, but also at band discontinuities at heterointerfaces, as will be reviewed in Section 4.1.

It is therefore possible to obtain the SCR width from its dependence on the applied bias, and furthermore, it follows from Eq. 88 that this information can be obtained from the analysis of the QE. The main difficulty in the analysis of Eq. 88 for the case of CGSe-based thin-film solar cells is the requirement of precise absorption data of samples

which are characterised by a considerable roughness. Furthermore, different combinations of w and L values result in similar QE curves, due to the proportionality between:

$$e^{\alpha(\lambda)w} \propto \frac{1}{1+\alpha(\lambda)L} \qquad \text{Eq. 100}$$

to first order in Taylor's expansion, and thus *all* factors in Eq. 88 are source of non-negligible errors in the real case. A way to overcome these difficulties and to simplify the numerical analysis is to make use of the concept of the *effective* diffusion length of minority carriers, commonly accepted in the research field of polycrystalline materials. Following the model derived by Klenk[109], Eq. 88 can be rewritten in terms of an effective diffusion length L_{eff}, defined as the sum of the SCR width plus the actual minority carrier diffusion length, as follows:

$$QE = K\left(1 - e^{\alpha(\lambda)L_{eff}}\right) \qquad \text{Eq. 101}$$

where K is a dimensionless factor accounting for optical losses (reflection and absorption in the window layer) and electronic losses due to interface recombination. One further advantage of this approach is thus the possibility of working directly with external QE values. The model assumes a complete collection of minority carriers within the SCR and neglects the influence of majority carriers in the collection function. Now, from the definition of the effective diffusion length:

$$w = L_{eff} - L_{diff} \qquad \text{Eq. 102}$$

it follows from Eq. 99:

$$\left(L_{eff}(V) - L_{diff} + d_b\right)^2 = d_b^2 + \frac{2\varepsilon\varepsilon_0}{qN_A}\left(E_g - \Delta E_c - \xi - \frac{Q_i d_b}{\varepsilon\varepsilon_0} + \frac{qd_b^2 N_b}{2\varepsilon\varepsilon_0} - qV\right) \qquad \text{Eq. 103}$$

The analysis of the QE measurements on the CGSe-based thin-film solar cells under different applied bias, to be presented in Chapter 4, will thus pursue the extraction of the effective diffusion length of minority carriers in the absorber from the fitting of the experimental curves, according to Eq. 101. The validity of the approach will be tested and accepted if a reasonable agreement between fit and experimental data can be obtained. The next step will include the separation of the two terms contributing to L_{eff}, according to Eq. 102, on the basis of the quadratic dependence of the SCR width on the applied bias, predicted by Eq. 103.

Prior to starting the analysis of the minority carrier diffusion length as explained above, minor corrections on the as-measured QE must be conducted, in particular those which include the effect of a non-negligible series resistance on the voltage drop at the active junction. Resistive components, like contact resistance at the electrodes and the material resistivity itself, consume part of the voltage drop applied to the device, the effect being

more important under high currents, as explained in the previous section[i]. Thus, it can not be excluded that a significant deviation between the nominal applied bias and the actual voltage drop at the p-n junction may be found, as result of the presence of resistive components other than the heterojunction and the SCR associated to it. This deviation can affect any further analysis based on the assumption that all the potential drops at the junction.

In order to check the influence of the series resistance on the measured QE values, the procedure reported by Phillips[110] will be followed. In the QE measurement the sample is illuminated with monochromatic light, as will be discussed in the experimental description below. This results in a change in the photocurrent density δJ_L, in the total current density δJ, and in the potential δV of the device, which according to Eq. 50 and neglecting the effects of a finite shunt resistance, leads to a total current density under forward bias given by:

$$J - \delta J = J_0 \exp\left(\frac{q((V+\delta V) - R_S(J-\delta J)}{AkT}\right) - J_L - \delta J_L \qquad \text{Eq. 104}$$

Subtracting Eq. 104 from Eq. 50 and expanding in series the exponential term for small δJ, we obtain:

$$\delta J_L = \left(1 + J_D \frac{q}{AkT} R_S\right)\delta J \qquad \text{Eq. 105}$$

where J_D is the dark current density of the diode. The experimental current δJ is thus reduced with respect to the actual photocurrent value. Since the QE is proportional to the current (Eq. 79), the same expression holds for QE measurements, which can thus be corrected for the effect of the series resistance according to:

$$QE_{corr} = QE_{\exp}\left(1 + J_D \frac{q}{AkT} R_S\right) \qquad \text{Eq. 106}$$

QE_{exp} denotes the experimental QE, and QE_{corr} the corrected value. Furthermore, with measurements performed under short-circuit conditions as reference, all measurements under bias can be referred to this reference case, following:

$$\frac{QE_{SC}}{QE_{bias}} = 1 + \frac{q}{AkT} R_S \left(J_{SC} - J_{bias}\right) \qquad \text{Eq. 107}$$

[i] These resistive elements were grouped and generically termed as the *series resistance* R_s in the equivalent circuit of Figure 10.

where J_{sc} and J_{bias} can be calculated from Eq. 79. Thus, the series resistance can be obtained from the linear fit of the QE ratio over the total current density difference in the cases of short circuit and voltage bias operation. An example of such procedure is shown in Figure 20 (left) where QE values were selected at an excitation wavelength of 710 nm.

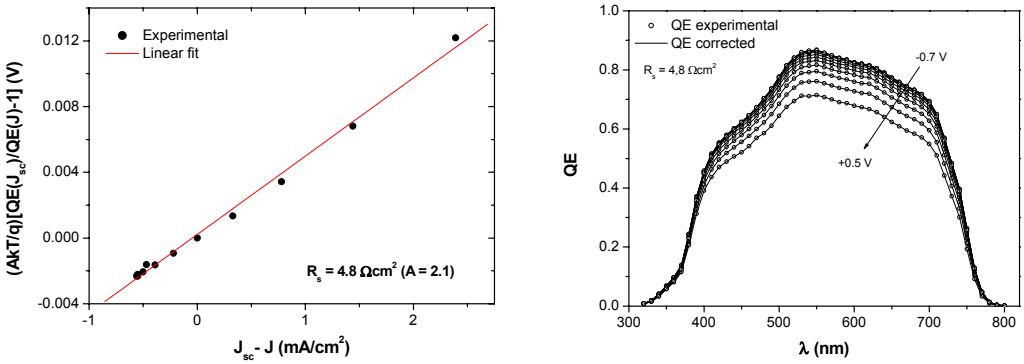

Figure 20. Calculated value of the series resistance R_S from QE measurements (λ=710 nm) under bias **(left)** and corrected values of QE from the extracted value **(right)**. The ideality factor A=2.1 was obtained from the J-V curve fit with the single diode model of Section 2.2.

In the case of CGSe-based devices it is found that the effect of series resistance on the QE yield is small over the range of applied bias (typically –0.7<V<+0.7) at room temperature, as inferred from minor deviations found between experimental and corrected QE values (shown in Figure 20 (right) after Eq. 107), in good agreement with studies on PVD-grown CGSe thin-film solar cells[66]. This is due to the relatively low current densities (J_{sc}~15 mA/cm^2) delivered by the wide gap CGSe material.

The experimental QE set up used in this work is shown schematically in Figure 21. It makes use of the lock-in principle, to account for intensity variations of the light source. This consists of a 120 W halogen and a 100 W Xenon-lamp, as in the case of the sun simulator described in the preceding section, covering the useful spectral range shown in Figure 15. The light is directed with a mirror to the entrance of the monochromator unit and chopped with an adjustable frequency (typically 60-70 Hz). The chopped signal (chopper reference signal) is monitored in an oscilloscope and recorded in the lock-in amplifier. The non-chopped beam is monochromatised and focused on the sample, placed on a movable sample holder. The sample is contacted in the four probe configuration, which allows for monitoring contact resistance at the front grids and the rear contact with a conventional multimeter. The photocurrent (sample signal) is first transformed into a voltage signal and amplified, and sent to the lock-in amplifier, which measures the phase difference between the reference and sample signals. The system is controlled from a computer, which stores the data. The QE of the sample under investigation is calculated by the ratio of the measured photocurrent to that obtained from a calibrated reference diode in an independent measurement. Depending on the wavelength range of interest, either a monocrystalline Si-diode alone, or in combination with a InGaAs-diode, are employed (Si for λ < 940 nm, InGaAs for λ > 940 nm).

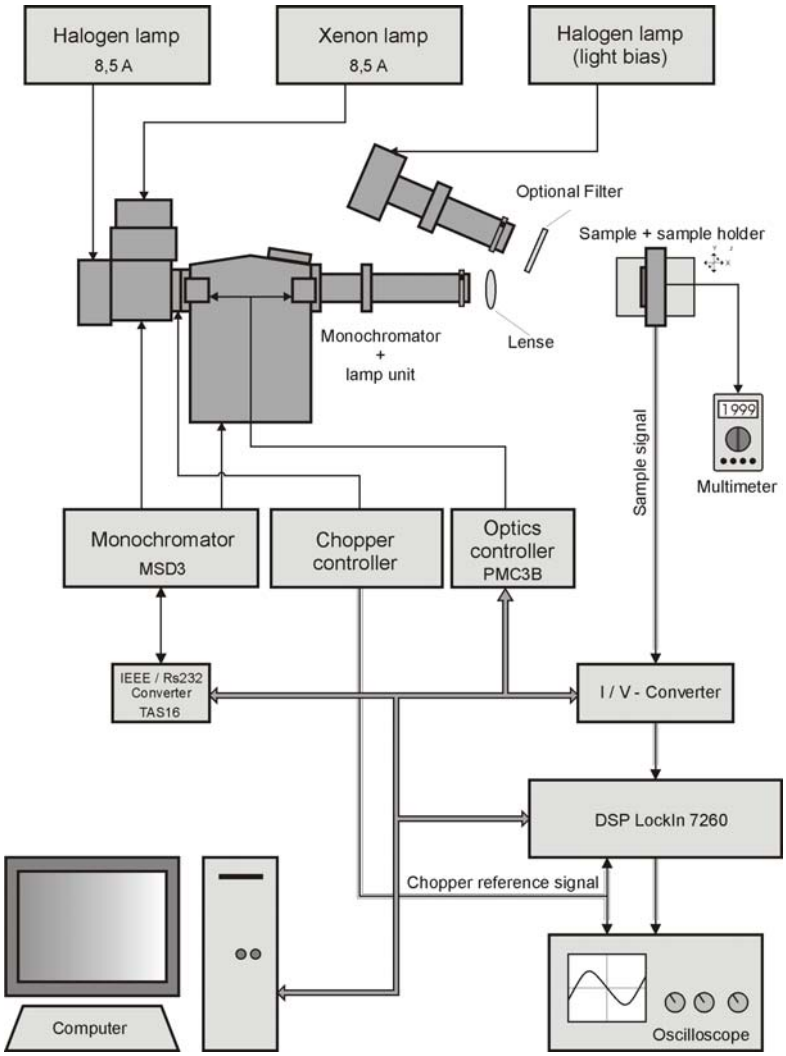

Figure 21. Schematic overview of the quantum efficiency set up, based on the lock-in principle. The light from the illumination source is chopped with an adjustable frequency (60-70 Hz). The chopped reference signal is monitored in an oscilloscope and recorded in the lock-in amplifier. The non-chopped beam is monochromatised and focused on the sample. The photocurrent (sample signal) is transformed into a voltage signal, amplified and sent to the lock-in amplifier, which measures the phase difference between the signals. The QE yield of the sample is calculated by the ratio of the measured photocurrent to that obtained from a reference sample (not shown) in an independent measurement.

2.3 The Kelvin Probe Force Microscope (KPFM)

Kelvin probe force microscopy (KPFM), as first reported by Weaver and Abraham[111] is a technique based on Atomic Force Microscopy (AFM) designed for the measurement of contact potential (CP) variations between a sample and a vibrating tip on a nanometre scale, in addition to the topography imaging common to other AFM methods. The

application of the method in UHV conditions allows the measurement of absolute work function values of samples, if the corresponding value of the cantilever is known. The KPFM is essentially a non-contact vibrating capacitor device, suitable for the characterisation of thin-film semiconductor heterostructures.

The measurement of the work function is based on the measurement of the electrostatic forces between the tip and the sample. The cantilever is oscillated at its resonance frequency with a constant amplitude and scanned over the sample at a constant distance. A voltage is applied between tip and sample, consisting of a dc-bias U_{dc} and an ac-voltage $U_{ac}\sin\omega t$ of frequency ω. As a result of these biasing conditions, an oscillating electrostatic force appears, inducing an additional oscillation of the cantilever with characteristic frequency ω. The general expression of such electrostatic force can be expressed as[112]:

$$F_{es} = -\frac{1}{2}\frac{\partial C}{\partial z}U^2(t) = -\frac{1}{2}\frac{\partial C}{\partial z}\left[U_{dc} - \frac{\Delta\Phi}{q} + U_{ac}\sin(\omega t)\right]^2 \qquad \text{Eq. 108}$$

where q is the elementary charge, C denotes the capacitance between tip and sample and ΔΦ/q the contact potential, i.e. the difference in work function between tip and sample. This expression can be rewritten as $F_{es}=F_{dc}+F_{\omega}+F_{2\omega}$ expanding the term in brackets, where:

$$F_{dc} = -\frac{\partial C}{\partial z}\left[\frac{1}{2}\left(U_{dc} - \frac{\Delta\Phi}{q}\right)^2 + \frac{U_{ac}^2}{4}\right] \qquad \text{Eq. 109}$$

$$F_{\omega} = -\frac{\partial C}{\partial z}\left(U_{dc} - \frac{\Delta\Phi}{q}\right)U_{ac}\sin(\omega t) \qquad \text{Eq. 110}$$

$$F_{2\omega} = \frac{\partial C}{\partial z}\frac{U_{ac}}{4}\cos(2\omega t) \qquad \text{Eq. 111}$$

The dc component F_{dc} contributes to the topographical signal, the term F_{ω} at the characteristic frequency ω is used to measure the CP and the contribution $F_{2\omega}$ can be used for capacitance microscopy. A scheme of the measurement principle is shown in Figure 22. The tip and the sample are characterised by different work functions. When both elements are brought in contact, a net electric current will flow between them until the Fermi levels are aligned, as discussed previously. An electrostatic force between tip and sample builds up, resulting from the net charge transfer. A lock-in amplifier is used to detect the cantilever oscillation at ω. The signal is minimised by applying the dc-bias, which corresponds to the CP between tip and sample, as deduced from Eq. 110. Recording U_{dc} as the tip scans the sample allows to map the CP. Absolute values of the sample work function can indeed be obtained if the tip is first calibrated against a reference sample of known work function, like a piece of highly oriented pyrolytic graphite (HOPG). Tuning the ac-frequency ω to the second resonance frequency of the cantilever results in an improved sensitivity and allows the independent and simultaneous imaging of topography and CP. An energy resolution down to 5 meV can

be obtained with ac-voltages of 100 mV and a lateral resolution of 20 nm. Further details can be found in Refs. [113,114].

Information about the electronics of semiconductor surfaces can be obtained by comparing CP measurements conducted in darkness to those performed under illumination of appropriate wavelength. By the surface photovoltage (SPV) method[115], the illumination is used to excite charge carriers from surface states, which reduce the band bending associated to depletion of free carriers in the near surface region of semiconductors, as will be discussed in Chapter 3.

The experimental KPFM set-up consists of a modified commercial Omicron AFM/STM operated in UHV ($p<10^{-10}$ mbar) with Pt/Ir-coated Si cantilevers, which are calibrated before and after every measurement to monitor any possible modification of the tip due e.g. to undesired collisions with the sample. Further details can be found in Ref. [114]. Measurements on CGSe films and related devices have been done in this work scanning either directly on the film surface or over sample cross-sections. In the latter case, the samples were prepared in a similar way as described for the case of TEM characterisation (see Section 2.1.3). Pieces of the sample were cut and glued face-to-face with conductive epoxy, in some cases introducing an intermediate Cu-foil for a work function cross-reference. The cross-sections were mechanically polished in order to provide a final roughness in the range of tens of nm for optimal scanning. Further details on the sputter-cleaning process subsequently conducted on the samples under study will be discussed in Chapter 3 (see also Ref. [140]).

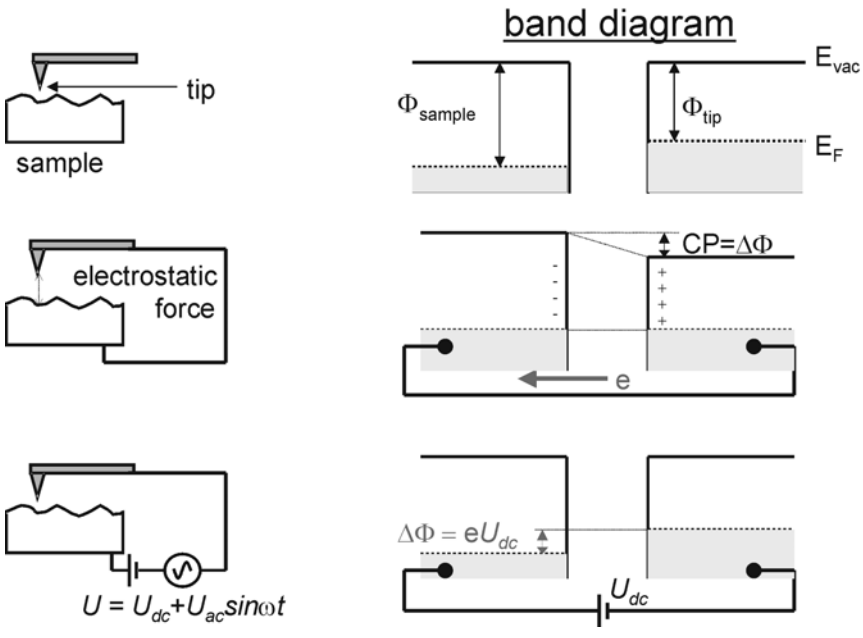

Figure 22. Operating principle of the KPFM for the measurement of the sample work function. The contact potential (CP) between tip and sample is recorded as the compensating U_{dc} bias, according to Eq.110.